Electric dipole spin resonance in a single- and two-electron quantum dot defined in two-dimensional electron gas at the $SrTiO_3/LaAlO_3$ interface

B. Szafran,[1,*] M. Zegrodnik,[2,†] M. P. Nowak,[2,‡] R. Citro,[3,§] and P. Wójcik[1,∥]

[1]*AGH University of Krakow, Faculty of Physics and Applied Computer Science, Al. Mickiewicza 30, 30-059 Krakow, Poland*
[2]*AGH University of Krakow, Academic Centre for Materials and Nanotechnology, Al. Mickiewicza 30, 30-059 Krakow, Poland*
[3]*Department of Physics E. R. Caianiello University of Salerno and CNR-SPIN, Via Giovanni Paolo II, 132, Fisciano (Sa), Italy*

(Received 22 December 2023; revised 3 April 2024; accepted 5 April 2024; published 25 April 2024)

We investigate the energy spectrum of a single- and two-electron quantum dot (QD) embedded in two-dimensional electron gas at the interface between $SrTiO_3$ and $LaAlO_3$, in the presence of the external magnetic field. For this purpose, the three-band model of $3d$ electrons defined on the square lattice of Ti ions was utilized. We demonstrate that, for the weak parabolic confinement potential, the low-energy spectrum is sufficiently well described by the effective Hamiltonian reduced to the one d_{xy} orbital with the spin-orbit interaction originating from the coupling to the d_{xz} and d_{yz} bands. This is not the case for stronger confinement where contribution of the states related to the $d_{xz/yz}$ orbital is relevant. Based on the time-dependent calculations, we discuss in detail the manipulation of the electron spin in a QD by external AC voltages, in the context of the electric dipole spin resonance. The allowed and forbidden transitions are discussed in detail with respect to the parity selection rule. Our calculations show that, for a single-electron QD, the spin flip in the ground state has the character of a Rabi resonance, while for two electrons, the singlet-triplet transition is forbidden by the parity symmetry. For the two-electron QD, we demonstrate that the spin-flip transition can still be accomplished via a second-order, two-photon process that has a two-state Rabi character for low AC field amplitude. The violation of the parity symmetry on the spin-flip transitions is also analyzed.

DOI: 10.1103/PhysRevB.109.155306

I. INTRODUCTION

The spin dynamics of electrons confined in quantum dots (QDs) has attracted increasing interest in recent years as a fundamental aspect for constructing spin qubits for future quantum information processing [1,2]. The key element in utilizing spin qubits in quantum technology is effective control of their states through coherent spin manipulation. In the case of a single QD, this can be realized through electron spin resonance-Rabi oscillations induced by external microwave radiation, which drives resonant transitions between the Zeeman-split energy levels in a magnetic field [3–5]. Alternatively, two-electron spin states in QDs have been demonstrated to be effectively tunable by exchange coupling [6].

A significant breakthrough in this field has been achieved in electrostatically defined QDs [7,8], where the microwave field has been successfully replaced by AC gate voltages [9,10]. Periodic changes in the potential induced by the AC field affect the spin of the confined electron through the momentum-dependent spin-orbit (SO) interaction [11,12]. This technique, called electric-dipole spin resonance (EDSR) [13–16], has been reported in two-electron double-QD systems using Pauli blockade of the current flow, which occurs when the dots are occupied by electrons with parallel spins [9,10].

The number of operations which can be performed on a spin qubit is a result of the switching time (mainly determined by the SO coupling strength) and the spin decoherence. The latter is strongly influenced by the host material, which sets the strength of hyperfine interaction (HFI) with nuclear spins as well as the coupling of the electron spin with the lattice vibrations and charge fluctuations via the SO interaction. Thus, the SO coupling, on the one hand, is responsible for coherent spin manipulations, but on the other hand, it is also the source of detrimental spin decoherence.

The two-dimensional electron gas (2DEG) formed at the interface between $SrTiO_3$ (STO) and other insulating transition metal oxides, such as $LaAlO_3$ (LAO) [17], is considered a promising material platform for QD-based spin qubits fabrication. The increasing interest in this platform is mainly because the considered 2DEG interface exhibits a unique combination of characteristics, including high mobility [18], large SO coupling [19,20], gate-tunable superconductivity [21–24], magnetic ordering [25], and ferroelectricity [26]. Its susceptibility to electrostatic gating, comparable with semiconductor materials, has brought significant advances in oxide-2DEG nanotechnology [27–30]. Authors of a recent study of single QDs based on LAO/STO have revealed the Coulomb blockade diamond characteristic for well-defined electrostatic confinement [27]. The electron spin in STO-based QDs can

---

[*] bszafran@agh.edu.pl
[†] michal.zegrodnik@agh.edu.pl
[‡] mpnowak@agh.edu.pl
[§] rocitro@unisa.it
[∥] pawelwojcik@agh.edu.pl

be controlled by large SO coupling, switched on and off by moderate gate voltages, which is hardly achievable with semiconducting platforms [19]. Note, moreover, that STO-based 2DEG is expected to have another significant advantage over semiconductors. It is characterized by a smaller impact of direct and indirect sources of decoherence, as the HFI with the nuclear spin bath should be suppressed by the $3d$ character of electrons—their wave functions have nodes at the nuclei positions [31]. All these properties, combined with the capability to interconvert charge and spin currents through Edelstein and spin Hall effects [32–35], exhibiting some of the highest efficiencies among solid-state materials, make LAO/STO-based QDs a promising platform for development of fast spin qubits with inherent scalability of 2D systems. However, so far, the electronic structure and spin dynamics in the STO-based QDs have not been systematically explored. Note that the structural lateral confinement of 2DEG at the $\mathrm{SrTiO_3/LaAlO_3}$ interface using nanolitography has also been applied [36] for formation of QDs.

In this paper, based on the three-band model, we investigate an electronic spectrum of single- and two-electron STO-based QDs. We derive the simplified one-band Hamiltonian for the d_{xy} orbital with inclusion of the SO interaction and demonstrate that it can sufficiently well describe the low-energy range of the spectrum for the low parabolic confinement. Based on the time-dependent scheme, we simulate the EDSR with the electron spin in a QD controlled by the AC electric field. The calculated transitions between states are discussed with respect to the direct (single-photon) and second-order (two-photon) processes determined by the parity symmetry of states. The organization of this paper is the following: in Sec. II, we present a theoretical model in the k-vector and real space as well as the simplified Hamiltonian for the d_{xy} band, Sec. II contains the analysis of the electronic spectra of single- and two-electron QDs as well as results of time-dependent simulations (EDSR). Finally, the summary and conclusions are included in Sec. IV.

II. THEORETICAL MODEL

A. Single-electron Hamiltonian for (001)-oriented LAO/STO interface

At the (001)-oriented LAO/STO interface, the conduction band is formed by the Ti t_{2g} orbitals (d_{xy}, d_{yz}, d_{xz}) coupled through $2p$ states of oxygen on the square lattice. At the interface, where a narrow quantum well is created [25,37,38] as a result of the polarization discontinuity, the degeneracy of the t_{2g} bands is lifted, resulting in 2D discrete states with the band d_{xy} being lower in energy with respect to the bands d_{yz} and d_{xz}. In wave-vector space, 2DEG at the (001) LAO/STO interface can be described by the Hamiltonian [39]:

$$\hat{H}_{\mathbf{k}} = \sum_{\mathbf{k}} \hat{C}^{\dagger}_{\mathbf{k}} (\hat{H}_0 + \hat{H}_{RSO} + \hat{H}_{SO} + \hat{H}_B)\hat{C}_{\mathbf{k}}, \tag{1}$$

where $\hat{C}_{\mathbf{k}} = (\hat{c}^{\uparrow}_{\mathbf{k},xy}, \hat{c}^{\downarrow}_{\mathbf{k},xy}, \hat{c}^{\uparrow}_{\mathbf{k},xz}, \hat{c}^{\downarrow}_{\mathbf{k},xz}, \hat{c}^{\uparrow}_{\mathbf{k},yz}, \hat{c}^{\downarrow}_{\mathbf{k},yz})^T$ corresponds to the vector of annihilation operators for electrons with spin $\sigma = \uparrow, \downarrow$ on the orbital d_{xy}, d_{xz}, d_{yz}, in the state $\mathbf{k}$. In Eq. (1), $\hat{H}_0$ describes the kinetic energy and is given by

$$\hat{H}_0 = \begin{pmatrix} \epsilon^{xy}_{\mathbf{k}} & 0 & 0 \\ 0 & \epsilon^{xz}_{\mathbf{k}} & \epsilon^{h}_{\mathbf{k}} \\ 0 & \epsilon^{h}_{\mathbf{k}} & \epsilon^{yz}_{\mathbf{k}} \end{pmatrix} \otimes \hat{\sigma}_0 \ , \tag{2}$$

with dispersion relations:

$$\begin{aligned} \epsilon^{xy}_{\mathbf{k}} &= 4t_l - 2t_l \cos k_x - 2t_l \cos k_y - \Delta_E , \\ \epsilon^{xz}_{\mathbf{k}} &= 2t_l + 2t_h - 2t_l \cos k_x - 2t_h \cos k_y , \\ \epsilon^{yz}_{\mathbf{k}} &= 2t_l + 2t_h - 2t_h \cos k_x - 2t_l \cos k_y , \end{aligned} \tag{3}$$

and the hybridization term defined by

$$\epsilon^{h}_{\mathbf{k}} = 2t_d \sin k_x \sin k_y . \tag{4}$$

In Eqs. (3) and (4), t_l and t_h are the hopping parameters (energies) for the light and heavy mass, and t_d is the energy which determines the coupling between the d_{xz}/d_{yz} bands. Due to the lack of the inversion symmetry occurring in a natural way at interfaces, LAO/STO-based 2DEG exhibits SO coupling, in this case, consisting of two components: the atomic and Rashba parts. The former appears as an effect of the atomic $\mathbf{L} \cdot \mathbf{S}$ interaction and can be expressed in the form [40]:

$$\hat{H}_{\mathrm{SO}} = \frac{\Delta_{\mathrm{SO}}}{3} \begin{pmatrix} 0 & i\sigma_x & -i\sigma_y \\ -i\sigma_x & 0 & i\sigma_z \\ i\sigma_y & -i\sigma_z & 0 \end{pmatrix} , \tag{5}$$

where Δ_{SO} determines the strength of the atomic SO energy, and σ_x, σ_y, σ_z are the Pauli matrices.

The Rashba-like SO term $\hat{H}_{\mathrm{RSO}}$, occurring as a result of the mirror symmetry breaking, is induced by the out-of-plane offset of atom positions at the interface and is given by

$$\hat{H}_{\mathrm{RSO}} = \Delta_{\mathrm{RSO}} \begin{pmatrix} 0 & i \sin k_y & i \sin k_x \\ -i \sin k_y & 0 & 0 \\ -i \sin k_x & 0 & 0 \end{pmatrix} \otimes \hat{\sigma}_0 \ , \tag{6}$$

where Δ_{RSO} determines the energy of the Rashba SO coupling.

Finally, the coupling of the external magnetic field to the spin and orbital momentum of electrons is considered by the Hamiltonian:

$$\hat{H}_B = \mu_B (\mathbf{L} \otimes \sigma_0 + g \mathbb{1}_{3\times 3} \otimes \mathbf{S}) \cdot \frac{\mathbf{B}}{\hbar}, \tag{7}$$

where μ_B is the Bohr magneton, g is the Landé factor, $\mathbf{S} = \hbar \boldsymbol{\sigma}/2$ with $\boldsymbol{\sigma} = (\sigma_x, \sigma_y, \sigma_z)$, and $\mathbf{L} = (L_x, L_y, L_z)$ with

$$L_x = \begin{pmatrix} 0 & i & 0 \\ -i & 0 & 0 \\ 0 & 0 & 0 \end{pmatrix}, \quad L_y = \begin{pmatrix} 0 & 0 & -i \\ 0 & 0 & 0 \\ i & 0 & 0 \end{pmatrix},$$
$$L_z = \begin{pmatrix} 0 & 0 & 0 \\ 0 & 0 & i \\ 0 & -i & 0 \end{pmatrix}. \tag{8}$$

In our calculations, we assume the tight-binding parameters $t_l = 875$ meV, $t_h = 40$ meV, $t_d = 40$ meV, and $\Delta_E = 47$ meV taken from Ref. [21], the Landé factor [41] $g = 3$, and the SO coupling parameters $\Delta_{\mathrm{SO}} = 10$ meV, $\Delta_{\mathrm{RSO}} = 20$ meV corresponding to that measured experimentally

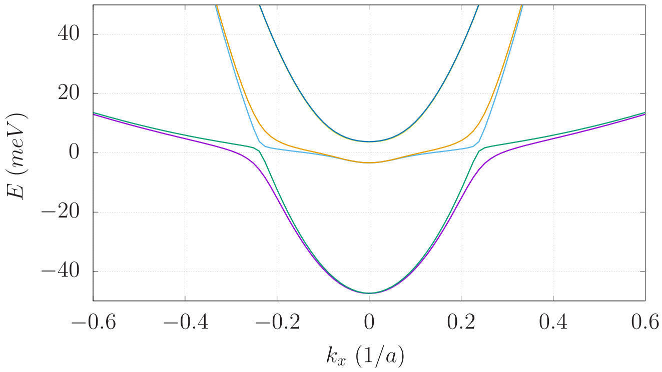

FIG. 1. Dispersion relation $E(k_x, k_y = 0)$ for the (001)-oriented LAO/STO heterostructures.

[19,20]. The dispersion relation $E(k)$ for the chosen parameters is presented in Fig. 1.

For confined nanostructures such as QDs, it is necessary to express the Hamiltonian in Eq. (1) in the real space. On the square lattice, with the position indexed by (μ, ν), the single-electron Hamiltonian in Eq. (1) takes the form:

$$\begin{aligned}\hat{H} &= \sum_{\mu,\nu}\hat{C}^{\dagger}_{\mu,\nu}(\hat{H}^0+\hat{H}_{SO}+\hat{H}_B)\hat{C}_{\mu,\nu}\\ &\quad+\sum_{\mu,\nu}\hat{C}^{\dagger}_{\mu+1,\nu}\hat{H}^x\hat{C}_{\mu,\nu}+\sum_{\mu,\nu}\hat{C}^{\dagger}_{\mu,\nu+1}\hat{H}^y\hat{C}_{\mu,\nu}\\ &\quad+\sum_{\mu,\nu}\hat{C}^{\dagger}_{\mu+1,\nu-1}\hat{H}_{mix}\hat{C}_{\mu,\nu}\\ &\quad-\sum_{\mu,\nu}\hat{C}^{\dagger}_{\mu+1,\nu+1}\hat{H}_{mix}\hat{C}_{\mu,\nu}+\text{H.c.},\end{aligned} \tag{9}$$

where $\hat{C}_{\mu,\nu} = (\hat{c}^{\uparrow}_{\mu,\nu,xy}, \hat{c}^{\downarrow}_{\mu,\nu,xy}, \hat{c}^{\uparrow}_{\mu,\nu,xz}, \hat{c}^{\downarrow}_{\mu,\nu,xz}, \hat{c}^{\uparrow}_{\mu,\nu,yz}, \hat{c}^{\downarrow}_{\mu,\nu,yz})^T$ corresponds to the vector of annihilation operators of electron with spin $\sigma = \uparrow, \downarrow$ on the orbital d_{xy}, d_{xz}, d_{yz} and the position (μ, ν), $\hat{H}^0$ defines the on-site energy related to the kinetic term and the confinement potential $V(\mathbf{r})$:

$$\begin{aligned}\hat{H}^0 &= \begin{pmatrix} 4t_l-\Delta_E & 0 & 0\\ 0 & 2t_l+2t_h & 0\\ 0 & 0 & 2t_l+2t_h\end{pmatrix}\otimes\hat{\sigma}_0\\ &\quad+\begin{pmatrix} V_{\mu,\nu} & 0 & 0\\ 0 & V_{\mu,\nu} & 0\\ 0 & 0 & V_{\mu,\nu}\end{pmatrix}\otimes\hat{\sigma}_0,\end{aligned} \tag{10}$$

while

$$\hat{H}^x = \begin{pmatrix} -t_l & 0 & 0\\ 0 & -t_l & 0\\ 0 & 0 & -t_h\end{pmatrix}\otimes\hat{\sigma}_0+\frac{\Delta_{\text{RSO}}}{2}\begin{pmatrix} 0 & 0 & -1\\ 0 & 0 & 0\\ 1 & 0 & 0\end{pmatrix}\otimes\hat{\sigma}_0, \tag{11}$$

$$\hat{H}^y = \begin{pmatrix} -t_l & 0 & 0\\ 0 & -t_h & 0\\ 0 & 0 & -t_l\end{pmatrix}\otimes\hat{\sigma}_0+\frac{\Delta_{\text{RSO}}}{2}\begin{pmatrix} 0 & -1 & 0\\ 1 & 0 & 0\\ 0 & 0 & 0\end{pmatrix}\otimes\hat{\sigma}_0, \tag{12}$$

$$\hat{H}_{\text{mix}} = \frac{t_d}{2}\begin{pmatrix} 0 & 0 & 0\\ 0 & 0 & 1\\ 0 & 1 & 0\end{pmatrix}\otimes\hat{\sigma}_0 \tag{13}$$

determines the energy of hopping to the nearest neighbors related to the kinetic energy and Rashba SO coupling in Eqs. (11), (12) as well as the hybridization in Eq. (13). In Eq. (9), $\hat{H}_{\text{SO}}$ and $\hat{H}_B$ have the same form as in the wave-vector space formulation and are given by Eqs. (5) and (7).

B. Simplified Hamiltonian for the d_{xy} band

The position of the d_{xy} band on the energy scale lowered by Δ_E relative to the d_{yz}/d_{xz} bands, together with the low effective mass, may lead to the dominant role of d_{xy} states when the confinement of the QD is weak. In such a case, one can anticipate that the influence of the higher-lying bands, d_{yz} and d_{xz}, is negligible. It is essential to note that reducing the Hamiltonian in Eq. (1) solely to the d_{xy} part is not sufficient, as it overlooks the SO coupling arising from the interaction with the $d_{xz/yz}$ bands via the terms H_{RSO} and H_{SO}. For this reason, more sophisticated methods are required to reduce the full Hamiltonian to the effective one describing the d_{xy} band. To derive it, let us express the Hamiltonian in Eq. (1) in the following form:

$$\hat{H} = \begin{pmatrix} \hat{H}_{xy} & \hat{H}_c\\ \hat{H}_c^{\dagger} & \hat{H}_{xz/yz}\end{pmatrix} - \Delta_E \mathbb{1}_{6\times 6}, \tag{14}$$

where

$$\hat{H}_{xy} = \begin{pmatrix} \epsilon^{xy}_{\mathbf{k}}+\Delta_E & 0\\ 0 & \epsilon^{xy}_{\mathbf{k}}+\Delta_E\end{pmatrix} + \frac{1}{2}g\mu_B\mathbf{B}\cdot\boldsymbol{\sigma}, \tag{15}$$

$$\hat{H}_{xz/yz} = \begin{pmatrix} \epsilon^{xz}_{\mathbf{k}}+\Delta_E & 0 & 0 & 0\\ 0 & \epsilon^{xz}_{\mathbf{k}}+\Delta_E & 0 & 0\\ 0 & 0 & \epsilon^{yz}_{\mathbf{k}}+\Delta_E & 0\\ 0 & 0 & 0 & \epsilon^{yz}_{\mathbf{k}}+\Delta_E\end{pmatrix}, \tag{16}$$

while the coupling between the states d_{xy} and d_{xz}/d_{yz} is given by

$$\begin{aligned}\hat{H}_c &= \frac{\Delta_{\text{SO}}}{3}\begin{pmatrix} 0 & i & 0 & -1\\ i & 0 & 1 & 0\end{pmatrix}\\ &\quad+ i\Delta_{\text{RSO}}\begin{pmatrix} \sin k_y & 0 & \sin k_x & 0\\ 0 & \sin k_y & 0 & \sin k_x\end{pmatrix}.\end{aligned} \tag{17}$$

Note that, in $\hat{H}_{xz/yz}$ we neglect the coupling of the bands d_{xz}/d_{yz} to the magnetic field and their hybridization assuming that the kinetic and SO energy constitute the major contribution to the energy.

Using the standard folding-down transformation, we can reduce the 6×6 model in Eq. (14) to the effective 2×2 Hamiltonian for the d_{xy} electrons:

$$\hat{H}^{\text{eff}}_{xy} = \hat{H}_{xy} + \hat{H}_c(\hat{H}_{xz/yz} - E)^{-1}\hat{H}_c^{\dagger}. \tag{18}$$

If we assume that Δ_E is much larger than the kinetic energy in the d_{xz}/d_{yz} band, we can expand $(\hat{H}_{xz/yz} - E)^{-1}$ from Eq. (18) into the Taylor series:

$$(\hat{H}_{xz/yz} - E)^{-1} = \frac{1}{\epsilon^{xz/yz}_{\mathbf{k}} + \Delta_E - E}\mathbb{1}_{4\times 4} \approx \frac{1}{\Delta_E}\mathbb{1}_{4\times 4}. \tag{19}$$

Then the effective Hamiltonian is reduced to the following form:

$$\hat{H}^{\rm eff}_{xy} = \left[\epsilon^{xz}_{\mathbf{k}} + \frac{2\Delta_{\rm SO}\gamma}{3(1-\gamma)}\right]\mathbf{1}_{2\times 2} + \frac{1}{2}g\mu_B\mathbf{B}\cdot\boldsymbol{\sigma} + \alpha(\sigma_y \sin k_x - \sigma_x \sin k_y), \tag{20}$$

where $\gamma = \Delta_{\rm SO}/3\Delta_E$ and $\alpha = \Delta_{\rm SO}\Delta_{\rm RSO}/3\Delta_E$. The last term in Eq. (20) is related to the SO coupling of the Rashba type [12,42], like that observed in semiconductor 2DEGs. It clearly demonstrates that the SO coupling for the d_{xy} band results from the relative interplay between the atomic and Rashba coupling through the bands d_{xz}/d_{yz}.

The Hamiltonian in Eq. (20) in the real space takes the form:

$$\begin{aligned}\hat{H}^{\rm eff}_{xy} = {} & \sum_{\mu,\nu}\hat{C}^{\dagger}_{\mu,\nu}\left\{\left[4t_l - \frac{2\Delta_{\rm SO}\gamma}{3(1-\gamma)}\right]\sigma_0 \right. \\ & \left. + \frac{1}{2}g\mu_B\mathbf{B}\cdot\boldsymbol{\sigma} + V_{\mu,\nu}\right\}\hat{C}_{\mu,\nu} \\ & + \sum_{\mu,\nu}\hat{C}^{\dagger}_{\mu+1,\nu}(-t_l\sigma_0 - i\alpha\sigma_y)\hat{C}_{\mu,\nu} \\ & + \sum_{\mu,\nu}\hat{C}^{\dagger}_{\mu,\nu+1}(-t_l\sigma_0 + i\alpha\sigma_x)\hat{C}_{\mu,\nu} + \text{H.c.},\end{aligned} \tag{21}$$

which, as we will show later, can be successfully used to describe the electronic structures of QDs with a weak confinement. In the above expression, $V_{\mu,\nu}$ corresponds to the confining potential of QD.

C. Integration of the two-electron problem

We consider the case of two electrons confined in a QD embedded in 2DEG at the (001)-LAO/STO interface, described by the Hamiltonian:

$$\hat{H}_2 = \hat{H}(1) + \hat{H}(2) + \frac{e^2}{4\pi\epsilon_0\epsilon r_{12}}, \tag{22}$$

where $\hat{H}$ is the single-electron Hamiltonian in Eq. (9) or in the simplified model reduced to the d_{xy} band, $\hat{H} = \hat{H}^{\rm eff}_{xy}$, see Eq. (21). We take the dielectric constant $\epsilon = 100\epsilon_0$ which is the upper limit of the electric field dependence of ϵ given in Ref. [43]. Although the dielectric constant of STO is known to be significantly dependent on the electric field and temperature, the assumed value is justified near the interface where the triangular quantum well is created and the electric field is large—see Appendix.

The problem is solved in the basis of antisymmetrized products of the single-electron eigenfunctions, i.e., in the exact diagonalization approach applied for an electron pair. For $H\Psi_q = E_q\Psi_q$, the single-electron eigenfunction is spanned over the $3d$ spin orbitals of a Ti ion:

$$\begin{aligned}\Psi_q(x,y,\sigma) &= \sum_j a^q_j d_j(x,y,\sigma) \\ &= \sum_{r_j,o_j,s_j} a^q_j d_{r_j,o_j}(x,y) S_{s_j}(\sigma),\end{aligned} \tag{23}$$

where the summation runs over the position of ions r_j, orbitals o_j on the ion, and the z component of the spin indexed by s_j; and S is the spin-up or spin-down eigenstate. In the sums, j is equivalent to the triple indices (r_j, o_j, s_j), and d_{r_j,o_j} is one of the $3d$ orbitals localized on the ion position r_j.

Evaluation of the matrix elements of the two-electron Hamiltonian requires determination of the Coulomb integrals:

$$\begin{aligned}I_{q_1q_2q_3q_4} &= \left\langle\Psi_{q_1}(1)\Psi_{q_2}(2)\right|\frac{1}{r_{12}}\left|\Psi_{q_3}(1)\Psi_{q_4}(2)\right\rangle \\ &= \sum_{j_1,j_2,j_3,j_4}\left(a^{q_1}_{j_1}a^{q_2}_{j_2}\right)^* a^{q_3}_{j_3}a^{q_4}_{j_4} \\ &\quad \times \left\langle d_{j_1}(1)d_{j_2}(2)\right|\frac{1}{r_{12}}\left|d_{j_3}(1)d_{j_4}(2)\right\rangle.\end{aligned} \tag{24}$$

The integral over the spin orbitals that appears in the sum is calculated based on the formula:

$$\begin{aligned}&\left\langle d_{j_1}(1)d_{j_2}(2)\right|\frac{1}{r_{12}}\left|d_{j_3}(1)d_{j_4}(2)\right\rangle \\ &\quad = \delta(r_{j_1},r_{j_3})\delta(r_{j_2},r_{j_4})\delta(s_{j_1},s_{j_3})\delta(s_{j_2},s_{j_4}) \\ &\quad\quad \times\left\{\left[1-\delta(r_{j_1},r_{j_2})\right]\frac{1}{|r_{j_1}-r_{j_2}|}\delta(o_{j_1},o_{j_3})\delta(o_{j_2},o_{j_4}) \right. \\ &\quad\quad \left. + \delta(r_{j_1},r_{j_2})\varepsilon(o_{j_1},o_{j_2},o_{j_3},o_{j_4})\right\},\end{aligned} \tag{25}$$

where

$$\varepsilon(o_{j_1},o_{j_2},o_{j_3},o_{j_4}) = \left\langle d_{j_1}(1)d_{j_2}(2)\right|\frac{1}{r_{12}}\left|d_{j_3}(1)d_{j_4}(2)\right\rangle \tag{26}$$

is the integral for the four orbitals localized on the same ion. The Kronecker deltas in the second line in Eq. (25) introduce the two-center approximation [44] and the orthogonality of the spin states. The third line is responsible for the contributions to the integral with the first and second electrons occupying different ions. In this term, we assume that the Coulomb potential changes slowly, allowing us to use the orthogonality of the orbitals. The last line of Eq. (25) is responsible for the Coulomb integrals over the same ion with electrons occupying various orbitals—that is denoted as the ε integral. This integral is evaluated using the Monte Carlo technique. For orbitals numbered as $d_{xy} = N\exp(-Z^*r/3)xy \rightarrow 1$, $d_{xz} = N\exp(-Z^*r/3)xz \rightarrow 2$, and $d_{yz} = N\exp(-Z^*r/3)yz \rightarrow 3$, using the hydrogenlike $3d$ orbitals with the normalization factor N and the effective atomic number $Z^* = 3.65$ given by the Slater rules for the Ti orbitals, the nonzero values of the on-site Coulomb integral are $\varepsilon(i,i,i,i) = 0.336$, $\varepsilon(i,j,i,j) = 0.306$, and $\varepsilon(i,j,j,i) = 0.015$ (for $i \neq j$) in atomic units. The remaining 12 integrals with other sequences of orbitals are zero due to negative parity of the integrated functions.

In the calculations, we use up to 50 lowest-energy single-electron states that produce 1225 Slater determinants as a basis for the two-electron problem.

D. Time evolution

For discussion of spin dynamics in the external electric field, we assume a periodic perturbation of the potential $V_{\rm AC}(t) = -eFx\sin(2\pi\omega t)$. We solve the Schrödinger equation with the time-dependent Hamiltonian $\hat{H}_t = \hat{H} + V_{\rm AC}(t)$. The solution is obtained on the basis of time-independent

Hamiltonian eigenstates $\Psi(t) = \sum_m c_m(t)\exp(-iE_nt/\hbar)|m\rangle$, with $\hat{H}|m\rangle = E_m|m\rangle$. Upon substitution of this wave function into the Schrödinger equation followed by a projection on the $\langle n|$ state, we obtain a system of equations for $c_n(t)$:

$$i\hbar c_n'(t) = -eF\sum_m c_m(t)\exp\left[i(E_n - E_m)\frac{t}{\hbar}\right] \times \sin(2\pi\omega t)\langle n|x|m\rangle, \quad (27)$$

which is solved using the Crank-Nicolson scheme. In the initial condition, we take $c_n(t=0) = \delta_{n,1}$. We monitor the maximal occupation ($\max|c_n(t)|^2$) of the excited states during the simulation that covers a time interval of 5 ns.

The present model assumes that the QD is a closed system subject to external fields; hence, no decay and dephasing mechanisms are considered. In QDs, the decay or relaxation of the system from the excited state to the ground state with opposite spin occurs with electron-acoustic phonon coupling in the presence of the SO interaction. In terms of the EDSR experiments, the problem was studied in Ref. [45]. The relaxation may induce off-resonant transition to a third state with a lower energy than the couple participating in the EDSR. This situation corresponds particularly to the double QD, when the states participating in the EDSR are two spin states of charge configuration corresponding to separated charges and the third state—lower in energy—with both electrons in the deeper dot. In this paper, with a single QD considered, there is no third state of a lower energy that could appear in the time evolution. In the simulations described in this paper, the ground state is always the initial state of the EDSR process.

The main source of the spin decoherence in III-V or Si QDs is the coupling of the electron spins with the nuclear spin bath via the HFI. In terms of the EDSR experiments, this decoherence leads to a reduction of the spin oscillations as a function of time [46]. Here, STO-based 2DEGs are expected to be characterized by a smaller decoherence, as the HFI with the nuclear spin bath is intrinsically low in STO [47] since the electron bands at the Fermi level are built of $3d$ atomic orbitals which vanish at the nuclei. In addition to the spin decoherence, the evolution of the states can be perturbed by the charge noise. However, the latter is mitigated by a large dielectric constant.

III. RESULTS

A. Single confined electron

The Hamiltonian in Eq. (9) in the basis limited to the d_{xy} orbitals is equivalent to a single-band Hamiltonian with an isotropic electron effective mass of $m = \frac{\hbar^2}{2a^2t_l} = 0.286m_0$, where $a = 0.39$ nm is the lattice constant. Since the electrostatic confinement is typically parabolic near its minimum, we have considered single-electron spectra for the external potential in the form $V(x,y) = \frac{1}{2}m\omega_0^2r^2$, with $\hbar\omega_0 = 9.344$ meV, 18.689 meV, and 37.378 meV, defining the range of a low, moderate, and strong confinement, respectively. The spectra for a single confined electron are given in Fig. 2, for the case of the magnetic field applied perpendicular to 2DEG.

For the lowest confinement energy $\hbar\omega_0$ [Fig. 2(a)], the share of d_{xy} orbitals [Fig. 2(b)] in the low-energy part of the spectra is ~1 and the basis limited to d_{xy} orbitals [Fig. 2(c)] provides nearly exact results in the low-energy range. For $\hbar\omega_0 = 18.689$ meV [Figs. 2(e) and 2(f)], the states with low contribution of d_{xy} orbitals appear already ~40 meV above the ground state, and the limited basis [Fig. 2(g)] produces results close to exact ones only for a few lowest-energy states. For the strongest confinement [Figs. 2(i)–2(k)], only the two lowest-energy states can be described with the limited model. The last column of the plots [Figs. 2(d), 2(h), and 2(l)] shows the results obtained with the Hamiltonian in Eq. (21) reduced to the d_{xy} orbitals with SO coupling. Note that the simple limitation of the basis to the d_{xy} orbitals in the Hamiltonian in Eq. (9) [Figs. 2(c), 2(g), 2(k)] excludes all SO coupling interactions due to the absence of direct coupling between the $d_{xy,\uparrow}$ and $d_{xy,\downarrow}$ spin orbitals. On the other hand, the reduced model in Eq. (20) transfers the SO interactions originating from the coupling to d_{xz} and d_{yz} orbitals to the basis of d_{xy}. Although the energy difference between the two approaches is small, the SO interaction in the model reduced to the d_{xy} orbital is needed, as it allows for control of the electron spin using the electric field.

Now let us consider the transitions driven by the AC electric field oriented within the plane of confinement. Direct transitions between the ground state and the excited states are governed by the values of the dipole matrix elements. The values $x_{nm} = \langle n|x|m\rangle$ for $n = 1$ are listed in Table I for the magnetic field of 10 T oriented perpendicular to the confinement plane. The spin-flipping transition from the ground state to the first excited state 1 → 2 has a small but nonzero matrix element. The states 1 and 2 have opposite parity; hence, the matrix element for 1 → 2 transition is nonzero. The element is small since the integration of the matrix element involves products of the spin-up and spin-down contributions to both states, and their dominant spins are opposite.

The matrix elements for spin-conserving transitions to the third and fifth states are ~500 times larger than $\langle 1|x|2\rangle$. A direct spin-flipping transition to the fourth state and the direct spin-conserving transition to the sixth state are forbidden. There is a symmetry reason for the vanishing transition matrix elements to the fourth and sixth states. Note that the Hamiltonian in Eq. (9) commutes with a generalized diagonal parity operator $\Pi = \mathrm{diag}[P, -P, -P, P, P, -P, P]$, where P is the scalar parity operator $P\psi(r) = \psi(-r)$. As a result, each of the components of the eigenfunctions has a definite—even or odd—scalar parity. It means that, for a given orbital, the P parity of the spin-up and spin-down components is opposite. Moreover, for a given spin, the scalar parity of the d_{yz} and d_{xz} components is the same and opposite to the parity of the d_{xy} component. The eigenvalues of the Π parity for the lowest-energy levels are listed in Table I, and the spectrum with parity marked by colors is plotted in Fig. 3(a). The fourth and sixth states have the same parity as the ground state, leading to the vanishing dipole matrix element for each of the six components in the scalar product $\langle 1|x|n\rangle$, with $n = 4$ or 6.

Figure 4 shows the maximum occupation for the driving AC field of 1 mV/nm with the full (a) and reduced (b) Hamiltonians, defined by Eqs. (9) and (21), respectively. In Figs. 4(a) and 4(b), above the driving energy of 10 meV, we can see wide overlapping maxima due to the allowed

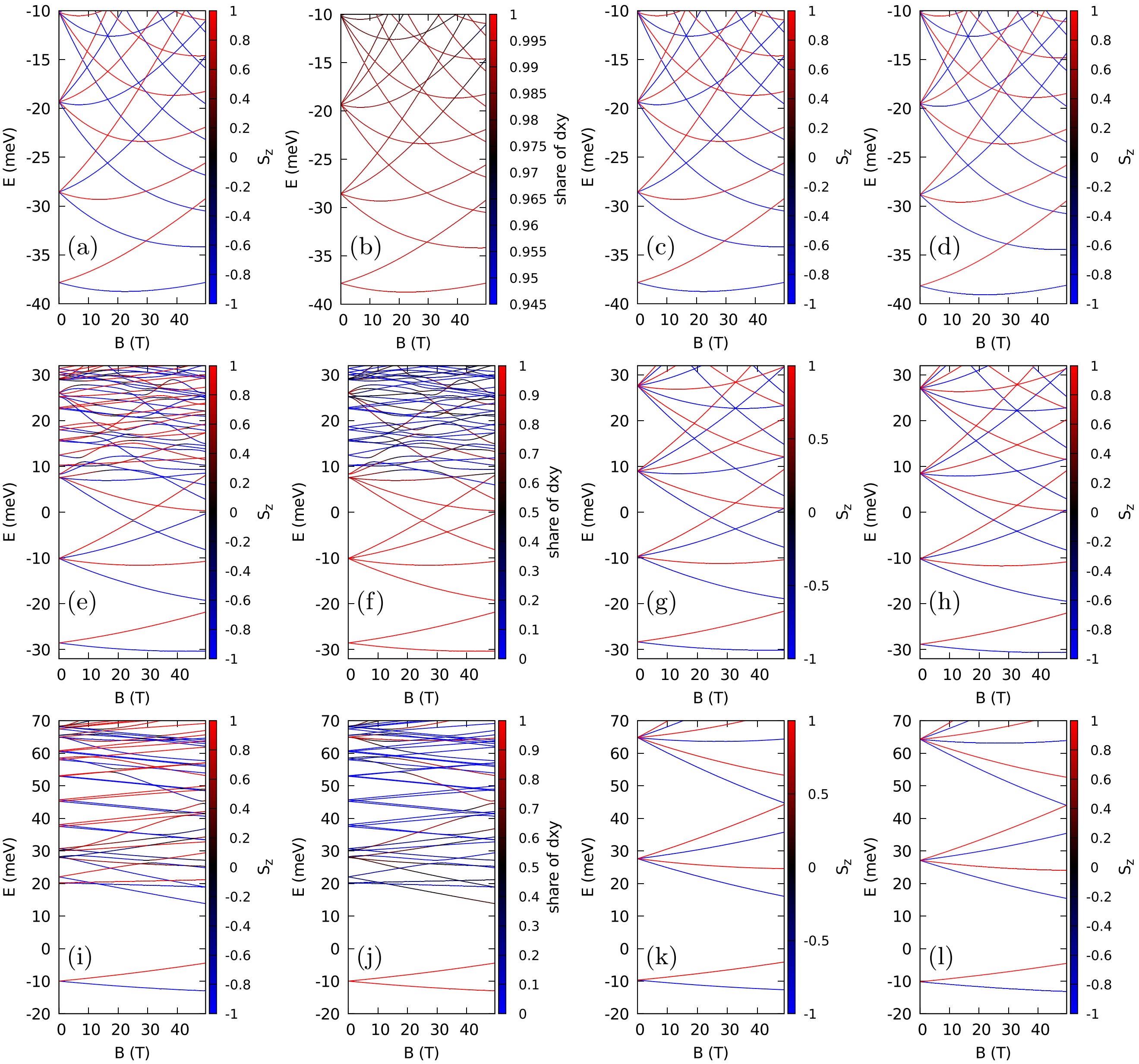

FIG. 2. Single-electron spectra as functions of the perpendicular magnetic field B, for parabolic confinement with energy (a)–(d) $\hbar\omega_0 = 9.344$ meV, (e)–(h) $\hbar\omega_0 = 18.689$ meV, and (i)–(l) $\hbar\omega_0 = 37.378$ meV. The left column of plots (a), (e), and (i) presents the results of the exact Hamiltonian in Eq. (9). The second column (b), (f), and (j) displays the share of d_{xy} orbitals with the wave functions of the states within the Hamiltonian in Eq. (9). The third column (c), (g), and (k) shows the spectra as obtained with the d_{xz} and d_{yz} orbitals excluded from the basis, still with the Hamiltonian in Eq. (9). The last column (d), (h), and (l) shows the results of the effective Hamiltonian in Eq. (21) reduced to the d_{xy} orbitals.

spin-conserving transitions to the third and fifth states [cf. Table I]. In the same energy range, the maximum occupancy of the seventh energy level is also observed. Note, however, that the direct transition 1 → 7 is forbidden by the parity symmetry, but the energy difference $E_7 - E_1$ is nearly equal to $2(E_3 - E_1)$, so the transition to the seventh energy level occurs through transitions via the third energy level $1 \rightarrow 3 \rightarrow 7$. In Fig. 4(a), the narrow yellow and red peaks ∼11 meV correspond to two-photon transitions to the sixth and ninth states, respectively, and appear at half the energy of the forbidden direct (i.e., single-photon) transition. The two-photon processes appear in the second-order time-dependent perturbation theory via a third state m that intermediates the transition between the initial and final states. In the second-order perturbation theory, the values of the coefficients in the wave function expansion are given by [48]

$$c_n(t) = c_n(0) + c_n^1(t) + c_n^2(t), \tag{28}$$

where

$$c_n^{(1)}(t) = \frac{-eF}{\hbar} x_{n1} \exp\left[i\frac{(\omega_{n1}-\omega')t}{2}\right] \frac{\sin\left(\frac{\omega_{n1}-\omega'}{2}t\right)}{(\omega_{n1}-\omega')}, \tag{29}$$

TABLE I. The energy levels (second column) for $\hbar\omega_0 = 18.689$ meV at $B = (0, 0, 10)$ T. The third column gives the parity Π eigenvalue. The dipole matrix element with the ground state and the nth eigenstate is given in the fourth column for an electric field of 1 mV/nm. The subsequent columns provide the contributions of the atomic spin orbitals to the Hamiltonian in Eq. (9) eigenstates.

n	$E + \Delta E$	Π	$\lvert eFx_{1n}\rvert$ (meV)	$d_{xy} \downarrow$	$d_{xy} \uparrow$	$d_{xz} \downarrow$	$d_{xz} \uparrow$	$d_{yz} \uparrow$	$d_{yz} \downarrow$
1	−29.30	−1	0	0.99493	0.00007	0.00085	0.00165	0.00085	0.00165
2	−27.57	1	0.00382	0.00010	0.99444	0.00186	0.00087	0.00186	0.00087
3	−12.72	1	1.866	0.98711	0.00019	0.00412	0.00223	0.00412	0.00223
4	−11.00	−1	0	0.00041	0.98529	0.00250	0.00465	0.00250	0.00465
5	−8.81	1	1.859	0.97891	0.00053	0.00783	0.00245	0.00783	0.00245
6	−7.08	−1	0	0.00039	0.97977	0.00313	0.00679	0.00313	0.00679
7	3.67	−1	0	0.95177	0.00103	0.01921	0.00438	0.01921	0.00438

and

$$c_n^{(2)}(t) = \frac{e^2F^2}{2i\hbar^2}\sum_m x_{nm}x_{m1}\left[\exp\left(i\frac{\omega_{nm}+\omega_{m1}-2\omega'}{2}t\right)\right.$$
$$\times\frac{\sin\left(\frac{\omega_{nm}+\omega_{m1}-2\omega'}{2}t\right)}{(\omega_{m1}-\omega')(\omega_{nm}+\omega_{m1}-2\omega')}$$
$$\left.-\exp\left(i\frac{\omega_{nm}-\omega'}{2}t\right)\frac{\sin\left(\frac{\omega_{nm}-\omega'}{2}t\right)}{(\omega_{m1}-\omega')(\omega_{nm}-\omega')}\right], \tag{30}$$

with $\omega' = h\omega/\hbar$ and $\omega_{nm} = (E_n - E_m)/\hbar$.

The formula for $c_n^{(2)}(t)$ involves a sum of the matrix-element products $x_{nm}x_{m1}$, with a resonance at $2h\nu = E_n - E_1$ (hence the two-photon nomenclature), due to the first term in brackets of Eq. (30). Although the direct (first-order) transitions $1 \to 6$ and $1 \to 7$ are forbidden by the same parity of the initial and final states, the two-photon process is still allowed due to nonzero values of matrix elements with $|m\rangle$ states of the opposite parity.

At a lower-energy range of Fig. 4(a), we notice a peak at $h\omega = 5.53$ meV for the transition to the third excited state. This in turn is a three-photon (third-order) process at the driving energy of $\frac{1}{3}$ of the energy difference between the energy levels (see Table I). The two-photon transition $1 \to 3$ is forbidden since the parity of any intermediate state m will agree with the parity of states 1 or 3, thus making one of the dipole matrix elements in the product equal to zero—see Eq. (30). The contributions of the separate eigenstates as a function of time for this transition is plotted in Fig. 4(d). The apparent large width of the lines results from rapid oscillations of the contributions $|c_3|^2$ and $|c_1|^2$. In Fig. 4(a), the peak does not exactly reach 1. In Fig. 4(c), we can see that the contribution of the seventh energy level reaches maximum at the same moment as the contribution of the third state, which limits the maximal value of the latter.

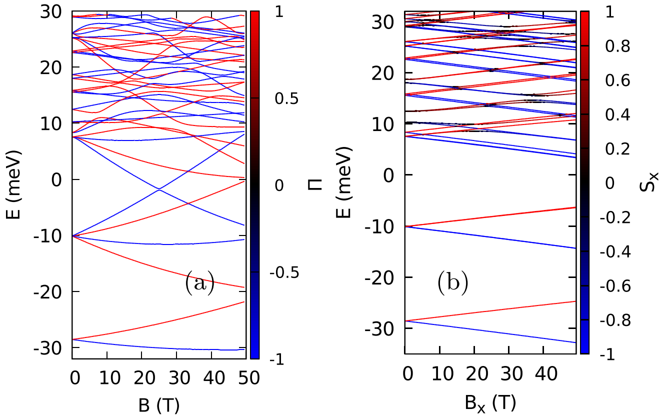

FIG. 3. (a) The single-electron spectrum of Fig. 2(e) ($\hbar\omega_0 = 18.688$ meV) but plotted with the colors indicating the Π parity of energy levels in a perpendicular magnetic field. The blue color stands for the negative parity and the red for the positive parity. (b) The single-electron spectrum with the same confinement energy but the external magnetic field oriented in the x direction. The colors indicate the sign of the x component of the spin.

The lowest-energy peak in Figs. 4(a) and 4(b) is the $1 \to 2$ spin-flipping transition near the driving energy of 1.727 meV—compare with Table I. This is the EDSR spin-flip transition that we focus on in this paper. We find that, at the resonance, for the amplitude of the electric field of $F = 1$ mV/nm, the spin inversion time is 537.9 ps, and for the amplitude decreased by half, the spin inversion time is twice longer—just as for the Rabi oscillation involving two states only. The time dependence of the contributions for this transition is given in Fig. 4(d). Note that, indeed, at the driving frequency for the spin flip, the higher-energy states have only a residual presence in the wave function; hence, the transitions can be identified as the Rabi resonance.

The reduced model incorporating the SO effects to the effective d_{xy} Hamiltonian in Eq. (21), presented in Fig. 4(b), produces similar results for the direct transitions, including the lowest-energy spin flip, and the structure of the wide maxima between 10 and 30 meV is similar. The matrix elements for the reduced model are given in Table II.

The estimated spin-flip time at the resonance for the amplitude of 1 mV/nm is 379.81 ps. Note, however, that the two-photon transitions to the sixth and eighth states as well as the three-photon transition to the third state of Fig. 4(a) are missing, as these transitions occur via the state with the d_{xz} and d_{yz} components. Moreover, a narrow peak corresponding to the transition to the seventh excited state at 8.4 meV in Fig. 4(b) is pronounced but missing in Fig. 4(a). In summary, the reduced model does not exactly reproduce the results of the full model for the higher-order transition processes that involve intermediate states between the initial and final states in terms of the time-dependent perturbation theory.

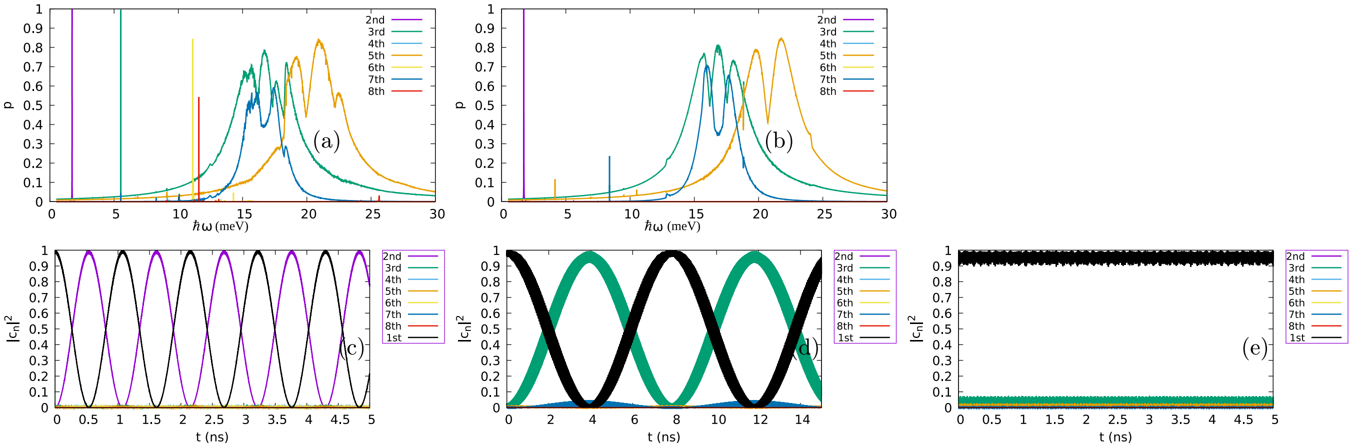

FIG. 4. The results of the integration of the time-dependent Schrödinger equation for $\hbar\omega_0 = 18.689$ meV, the perpendicular magnetic field of 10 T with the AC electric potential, $V_{\mathrm{AC}}(t) = -eFx\sin(\omega t)$. The simulation time is set to 5 ns and the amplitude of the electric field to 1 mV/nm. In (a) and (b), we plot the maximal occupancy of the nth state defined as maximal $|c_n(t)|^2$ over the simulation time. (a) shows the results for the Hamiltonian in Eq. (9) and (b) the results for the Hamiltonian in Eq. (21), reduced to the d_{xy} orbitals. We plot the results obtained with the full Hamiltonian as in (a). The lines show contributions of eigenstates as a function of time for (c) $\hbar\omega = 1.727$ meV, where the peak for the direct $1 \rightarrow 2$ transition is found in (a), (d) $\hbar\omega = 5.53$ meV, for the third-order transition peak $1 \rightarrow 3$ of (a), and (e) off-resonant excitation with $\hbar\omega = 10$ meV. In (c)–(e), we use the same colors for the same states as in (a) and (b). Additionally, in (c) and (e), we plotted the contribution of the ground state with the black line.

The spectrum of the reduced Hamiltonian misses part of the higher-energy states, which thus cannot assist in the transitions as the intermediates. Importantly, the EDSR transition between the lowest states with opposite spins is correctly captured by this simplified one-band model.

Finally, our calculations demonstrated that the spin flip from the ground state is only possible with the presence of both atomic SO and Rashba couplings. The hopping Rashba interaction is diagonal in spin and cannot drive spin transitions by itself. On the other hand, the atomic SO coupling does not couple the d_{xy} spin-up and spin-down orbitals which dominate in the lowest-energy spectrum. Therefore, only a mutual presence of both SO interactions opens the way for spin flips.

The manipulation of the spin with an electric field is also possible for the magnetic field oriented within the plane of confinement. Figure 3(b) shows the energy spectrum as a function of B_x. The second and third excited energy levels in Fig. 3(b) are nearly two times degenerate with a splitting of $\sim$0.01 meV at $B_x = 10$ T. At the scale of the figure, the lifting of the degeneracy is not resolved. For $B_x = 10$ T and the amplitude of the electric field of 1 mV/nm, the matrix element for the lowest-energy spin-flip transition induced by the AC electric field oriented in the x direction is 3.7 μeV. On the other hand, this matrix element is 0 for the AC field oriented in the y direction. The role of the orientation of the AC field and the external magnetic field is characteristic for the Rashba 2D interaction $H_R = \alpha_R(k_y\sigma_x - k_x\sigma_y)$ [12,42], which translates the motion in the y (x) direction into an effective magnetic field oriented along the x (y) axis [49]. The external magnetic field $(B_x, 0, 0)$ polarizes the spin parallel or antiparallel to the x direction. Then the motion induced by the AC electric field parallel to the x direction induces the y component of the magnetic field that induces the spin flips [49]. On the other hand, the AC field oriented in the y direction produces an effective magnetic field oriented parallel or antiparallel to the external magnetic field. It can only affect the spin-splitting energy but does not couple the states with spins oriented in opposite directions along the x axis.

TABLE II. Same as Table I only for the d_{xy}-reduced Hamiltonian in Eq. (21).

n	$E + \Delta E$	Π	$\lvert eFx_{12}\rvert$ (meV)	$d_{xy} \downarrow$	$d_{xy} \uparrow$
1	17.404	−1	0	0.9998	0.0002
2	19.139	1	0.0054	0.00029	0.99971
3	34.157	1	1.80	0.99960	0.0004
4	35.899	−1	0	0.00049	0.99951
5	38.198	1	1.880	0.99951	0.00049
6	39.922	−1	0	0.00058	0.99942
7	50.901	−1	0	0.00069	0.99931

The analysis given above describes the spin-flipping transitions for the energy difference between the low- and high-spin states of a few meV. Note, however, that EDSR experiments [2] are usually performed with the AC field applied to the gate electrodes in a microwave range of $\sim$10 GHz, which corresponds to the spin-splitting energy of $\sim$0.041 meV. For the single-electron spectrum with $\hbar\omega_0 = 18.689$ meV [cf. Figs. 2(e)–2(h)], this energy difference between the spin-down ground state and the spin-up first excited state corresponds to the magnetic field of the magnitude $B_z = 0.24$ T for which the dipole matrix elements $\langle 1|eFx|2\rangle$ are lower than at $B_z = 10$ T. The dependence of $\langle 1|eFx|2\rangle$ on the magnetic field is presented in Fig. 5(a). Note that the transition matrix element $\langle 1|eFx|2\rangle$ is calculated by summation of the integrals over the six spin-orbital channels. We find that, at $B = 0$, the sum of components integrated over the spin-up orbitals is exactly opposite to the ones integrated over the spin-down orbitals [see Fig. 5(a)]. In consequence, the transition matrix element at $B = 0$ is exactly zero. As B_z increases, the spin-down components are promoted by the spin Zeeman effect so that

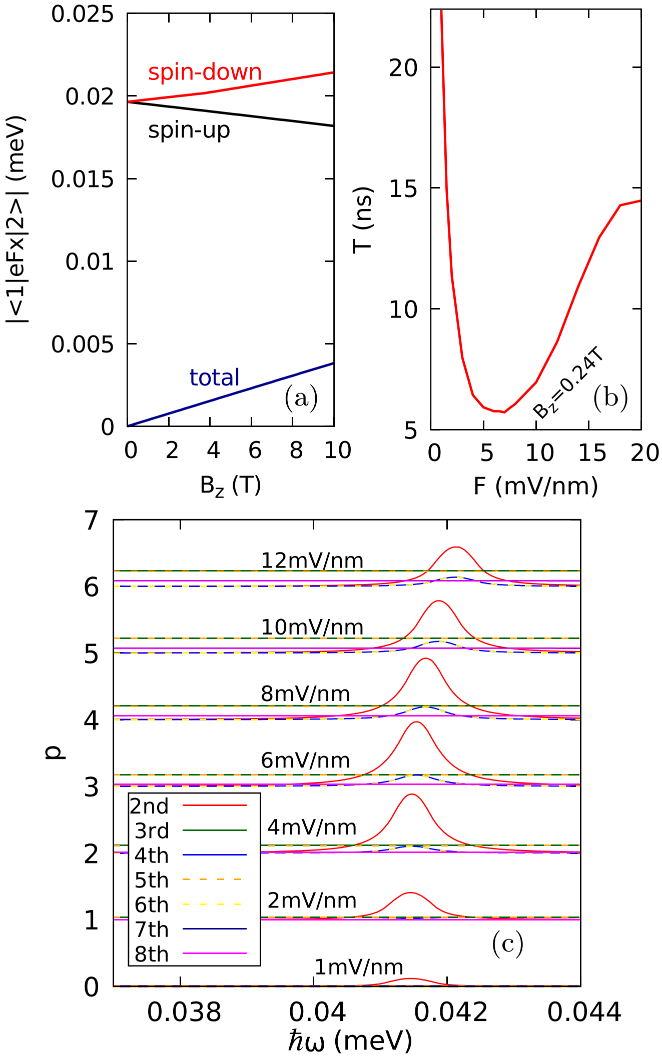

FIG. 5. The results for the single-electron and confinement energy $\hbar\omega_0 = 18.688$ meV. (a) The absolute value of the dipole matrix element for AC field of $F = 1$ mV/nm (blue line) and the absolute values of the contributions to the matrix element from the spin-up and spin-down components. These contributions have opposite sign and exactly cancel each other at $B = 0$. (b) The spin-flip time as a function of the AC amplitude for $B_z = 0.24$ T, where the energy splitting between the ground (spin-down) and the first excited state (spin-up) is ~0.0414 meV, which corresponds to the microwave frequency of ~10 GHz. (c) The maximal occupancy of the lowest-energy levels for the time evolution starting from the ground state and lasting 5 ns. The AC field amplitude increases from the bottom to the top. The subsequent plots for higher amplitudes are shifted by +1 each.

the contributions to the matrix element from both the spin channels become unequal, which results in the nonzero value which changes a linear function of the external magnetic field [Fig. 5(a)]. For the chosen magnetic field $B_z = 0.24$ T and $F = 1$ mV/nm, we estimate the spin-flip time equal to 22.36 ns (compare with the spin-flip transition at 10 T discussed in Sec. III A, which is 537.9 ps only). The spin-flip time can be shortened by applying AC field of the larger amplitude. Note, however, that the increased amplitude of the AC field may lead to appearance of the higher-energy states and changes the nature of the transition from the Rabi resonance to a more complex dynamics. The spin-flip time as a function of the amplitude is plotted in Fig. 5(b) and the maximal occupancy of the states in Fig. 5(c). We find that the shortest spin-flip time of 5.71 ns is found near $F \simeq 7$ mV/nm. Interestingly, the spin-flip time is an inverse function of the matrix element—as in the Rabi oscillation—only for $F < 4$ mV/nm. At larger F, the third and fifth states (both spin-down) appear over the entire studied range of $\hbar\omega$—see Fig. 5(c). Importantly, the fourth and sixth states (both spin-up) appear within the range of the resonant spin-flip maximum, which indicates that the electron is first transferred to the second energy level and next strongly couples to higher spin-up energy states [50]. Note that the spin-flip resonance in Fig. 5(c) is blueshifted for a higher AC field amplitude. This effect is known as the Bloch-Siegert shift [51].

B. Two confined electrons

1. Spectra

The energy spectra for the confined electron pair are displayed in Fig. 6, for the exact Hamiltonian in Eq. (9) (first three columns of plots) and the effective Hamiltonian in Eq. (21). In the third column, the basis was limited to solely d_{xy} orbitals in the Hamiltonian in Eq. (9). The effective Hamiltonian (fourth column) and the limited basis applied to the exact Hamiltonian (third column) produce similar results although with a small shift on the energy scale. The splitting between the energy levels that moves parallel in the magnetic field is smaller in the exact Hamiltonian (the first column in Fig. 6) than in the approximate approaches (the last two columns in Fig. 6). The share of d_{xy} orbitals in the low-energy states depends on the energy eigenvalue and the strength of confinement similarly as in the single-electron case (cf. Fig. 2).

In the following, we are mainly interested in the spin flip between the spin-singlet ground state and the first excited triplet state with the spins polarized antiparallel to the external magnetic field. The contributions of the orbitals, the parity, and the dipole matrix elements are given in Table III for $\hbar\omega_0 = 18.688$ meV and the perpendicular magnetic field of 12 T. In the table, we see that the transition of main interest $1 \rightarrow 2$ is forbidden by the parity symmetry, while the transitions are allowed to the pairs of even Π parity states—the third and fourth as well as the seventh and eighth. Each pair is split by ~1 meV, and the energy levels of the pair move parallel when the magnetic field is changed [Fig. 6(e)]. In each pair, the transition to a lower-energy state has a much smaller probability than to a higher-energy one which can be explained as follows. In the basis limited to d_{xy} orbitals (third column in Fig. 6), the spatial and spin degrees of freedom separate due to the absence of the SO coupling effects. Then the lower-energy state corresponds to the spin triplet with spin z component equal to zero and the antisymmetric spatial wave function. The higher-energy state corresponds to the symmetric spatial wave function characteristic to the spin singlet.

The matrix elements for the transition from the singlet ground state calculated with the $x_1 + x_2$ operator are then zero due to the antisymmetry of the spatial part of the wave function with respect to the electrons interchange. The lifting

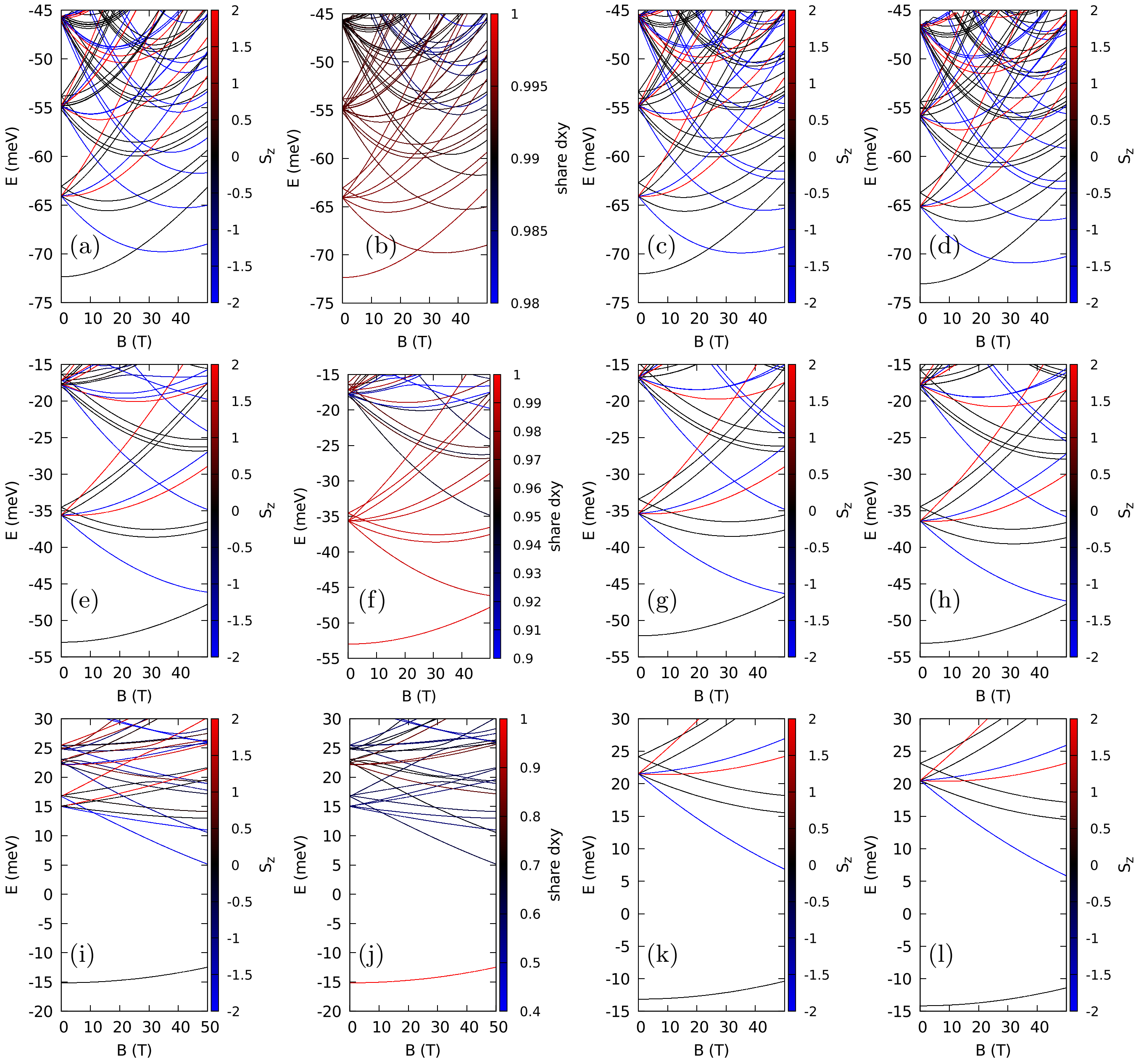

FIG. 6. Energy spectra for a confined electron pair (a)–(d) $\hbar\omega_0 = 9.344$ meV, (e)–(g) $\hbar\omega_0 = 18.689$ meV, and (h)–(l) $\hbar\omega_0 = 37.378$ meV. The first column of the plots shows the results of the full model Hamiltonian in Eq. (9). The color on the first, third, and fourth (second) columns corresponds to the component of the total spin (share of d_{xy} orbitals). The third column shows the spectra for the Hamiltonian in Eq. (9) but with the basis limited to d_{xy} orbitals. The last column presents the results for the d_{xy}-reduced Hamiltonian in Eq. (21), with the spin-orbit (SO) coupling effects integrated into the d_{xy} band.

of the separation between the spin and the space by the SO interaction included in the complete basis opens the direct channel for the transition to the lower-energy level of each pair, but the matrix element for the lower-energy state is small.

The results of the time evolution in the $V_{\mathrm{AC}}(t)$ field are plotted in Fig. 7 where, for the AC amplitude of 0.5 mV/nm, we can see wide maxima corresponding to the direct transitions to the fourth and eighth states. In addition to the wide maxima, we can observe a peak for the direct transition to the seventh state near $\hbar\omega = 20$ meV. Two narrow peaks corresponding to the transition to the third state appear near $\hbar\omega = 15$ meV, and next, we see a third-order transition to the eighth state. The second-order transition to this state is forbidden by the symmetry (cf. Table III). To the left of this peak, there is the lower one due to the two-photon transition of main interest: to the second energy level—the one which corresponds to the flip of one of the spins from the ground state for which the direct transition is forbidden by the parity symmetry.

For the amplitude of the AC field increased to 1 mV/nm [Fig. 7(b)], the spin-flip 1 → 2 transition probability within 5 ns of the simulation is increased to 98.8% via the second-order two-photon process that takes 4.7 ns. For comparison,

TABLE III. Results for two electrons, confinement energy $\hbar\omega_0 = 18.688$ meV, and the vertical magnetic field of 12 T. The results are organized as in Table I for a single electron.

n	$E + \Delta E$	Π	$\lvert -eFx_{1n}\rvert$ (meV)	$d_{xy}\downarrow$	$d_{xy}\uparrow$	$d_{xz}\downarrow$	$d_{xz}\uparrow$	$d_{yz}\uparrow$	$d_{yz}\downarrow$
1	−52.276749	−1	0	0.995	0.994	0.00279	0.00252	0.00279	0.00252
2	−39.169408	−1	0	1.982	0.000	0.00484	0.00381	0.00484	0.00381
3	−37.100982	+1	0.0097	0.991	0.990	0.00463	0.00461	0.00463	0.00461
4	−36.026479	+1	2.63	0.991	0.990	0.00462	0.00457	0.00463	0.00457
5	−35.032511	−1	0	0.001	1.979	0.00444	0.00538	0.00444	0.00538
6	−34.466481	−1	0	1.972	0.001	0.00927	0.00409	0.00927	0.00409
7	−32.389505	+1	0.0149	0.986	0.987	0.00727	0.00607	0.00727	0.00607
8	−31.313806	+1	2.62	0.987	0.987	0.00718	0.00613	0.00718	0.00613

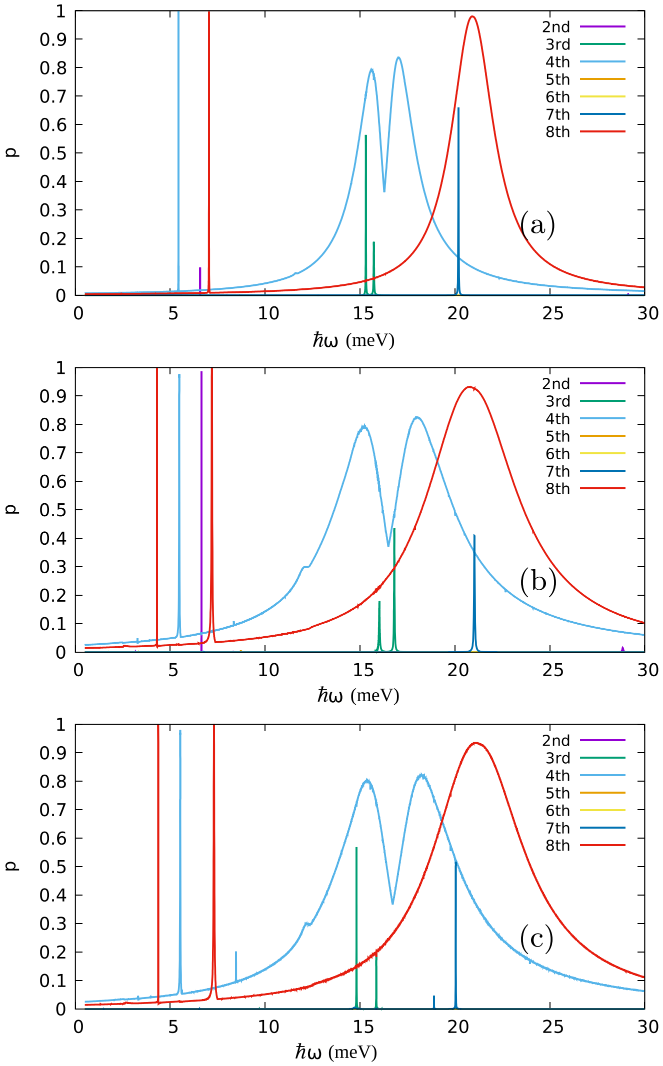

FIG. 7. The results for two electrons, confinement energy $\hbar\omega_0 =$ 18.688 meV, and the vertical magnetic field of 12 T. Maximal occupation probability of excited states for the ground state as the initial one in the time evolution lasting 5 ns for AC potential $V_{\mathrm{AC}} = -eFx\sin(2\pi\omega t)$ with the amplitude (a) 0.5 mV/nm and (b) and (c) 1 mV/nm. (a) and (b) show the results of the full model, while results for the effective Hamiltonian reduced to the d_{xy} orbitals in Eq. (21) are given in (c). The spin-flip transition $1 \rightarrow 2$ in the two-photon process takes 4.7 ns for $F = 1$ mV/nm.

for the AC field amplitude set at 0.5 mV/nm, the spin flip via the second-order process takes 24.7 ns, and the transition to the triplet state is achieved with the probability of 99.645%. The increased fidelity of the spin flip by reduction of the AC field amplitude is due to the reduction of the contribution of higher-energy states in the time evolution [cf. Figs. 7(a) and 7(b)]. Therefore, there is a tradeoff between the transition time and the fidelity. Note that, in the results for the effective Hamiltonian reduced to the d_{xy} orbitals, the peak due to the two-photon second-order spin-flipping transition to the second energy level is missing [Fig. 7(c)]. Although the reduced model worked well for the direct spin-inversion in the single-electron case, the second-order transition is missed out. In fact, a closer inspection of the results reveals the second-order peak but with a tiny magnitude of the order of 10^{-4}, which is outside the resolution of Fig. 7(c). Already in the single-electron case, we noticed that the reduced model is not completely reliable for the description of the higher-order transitions, which go via intermediate states, part of which are missing in the reduced Hamiltonian eigenspectrum.

The two-photon process for the spin-flip transition $1 \rightarrow 2$ is not very fast, and the direct one is missing due to the dipole matrix element that vanishes due to the parity symmetry reason. One can try to speed up the process by, e.g., perturbation of the confinement potential lifting its inversion symmetry and thus the parity selection rule. To lower the symmetry, we have placed a Gaussian perturbation $V_g = V_0 \exp\{-[(x-x_r)^2 + y^2]/s^2\}$, with $x_r = 3$ nm and $s = 2$ nm, to the parabolic confinement potential. The matrix elements for $V_0 = 2$ and 20 meV are listed in Table IV. We see that the largest transition elements to the fourth and eighth states are weakly changed by the Gaussian perturbation to the potential, while the transition from the ground state to the first excited state, involving a transition from zero to spin-polarized spin becomes nonzero in the presence of perturbation.

The two-electron energy spectra for the potential with the Gaussian perturbation are displayed in Fig. 8 for $V_0 = 2$ and 20 meV. The Gaussian perturbation opens avoided crossings between states of the same spin and the parity which is opposite for the symmetric potential. The transition spectra are plotted in Fig. 9 for $V_0 = 20$ meV and the AC field amplitude of 0.25 mV/nm (a), 0.5 mV/nm (b), and 1 mV/nm (c). In each panel, both first- and second-order spin-flipping transitions $1 \rightarrow 2$ are observed. As the amplitude of the AC field increases, the second-order peak near $\hbar\omega = 6$ meV grows

TABLE IV. The dipole matrix elements in meV for the two-electron system with the Gaussian perturbation to the harmonic oscillator potential with confinement energy $\hbar\omega_0 = 18.688$ meV and the vertical magnetic field of 12 T, for the amplitude of the AC electric potential eF of 1 mV/nm. The second (third) column gives the results for $V_0 = 2$ meV ($V_0 = 20$ meV). The fourth column lists the results for $V_0 = 20$ meV obtained with the reduced Hamiltonian.

n	$\lvert eFx_{1n}\rvert$, $V_0 = 2$ meV	$\lvert eFx_{1n}\rvert$, $V_0 = 20$ meV	← reduced mod.
1	0.1300	1.1726	1.1298
2	0.0006	0.0039	0.0013
3	0.0094	0.0058	0.0029
4	2.5800	2.0464	2.1145
5	0.0019	0.0094	0.0558
6	0.0011	0.0098	0.0042
7	0.0056	0.0054	0.0049
8	2.6800	3.0296	3.0039

up, but the first-order peak near $\hbar\omega = 12$ meV decreases. The decrease of the single-photon transition is due to the widening of the maxima related to transitions to the sixth and eighth states that compete in the evolution process with the transition to the second state. The spin-flip times for the second-order process for the AC amplitudes of 0.25, 0.375, 0.5, 0.75, and 1 mV/nm are 39.2, 17.7, 10.2, 4.9, and 3.09 ns, respectively. The maximal occupation of the second energy level are 99.9%, 99.6%, 99%, 98.7% and 97.7%, respectively. For the first-order transition, the spin-flip times are 2.25, 1.6, 1.4, 1.24, and 3.1 ns, with the fidelity of the transfer to the second excited state of 98.6, 96.9, 91.2, 90.6, and 83.7%. Remarkably, in this case, the spin-flip transition slows down when the amplitude is increased from 0.75 to 1 mV/nm, which is due to participation of the other excited states in the time evolution in addition to the initial and targeted ones. For both the second- and first-order transitions, the fidelity of the spin flip decreases with the AC amplitude due to leakage of the wave function to the higher-energy states. However, the fidelity of the transfer via the second-order processes is larger due to the lower background of the other excited states in the lower-energy range.

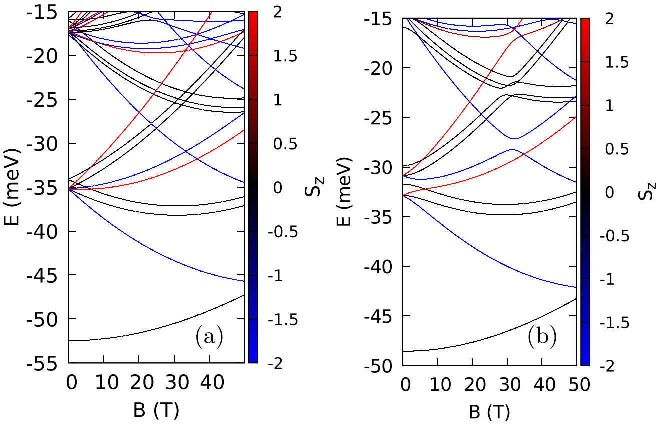

FIG. 8. The energy spectra for two electrons and the confinement energy $\hbar\omega_0 = 18.688$ meV in the presence of the off-center Gaussian perturbation with (a) $V_0 = 2$ meV and (b) $V_0 = 20$ meV.

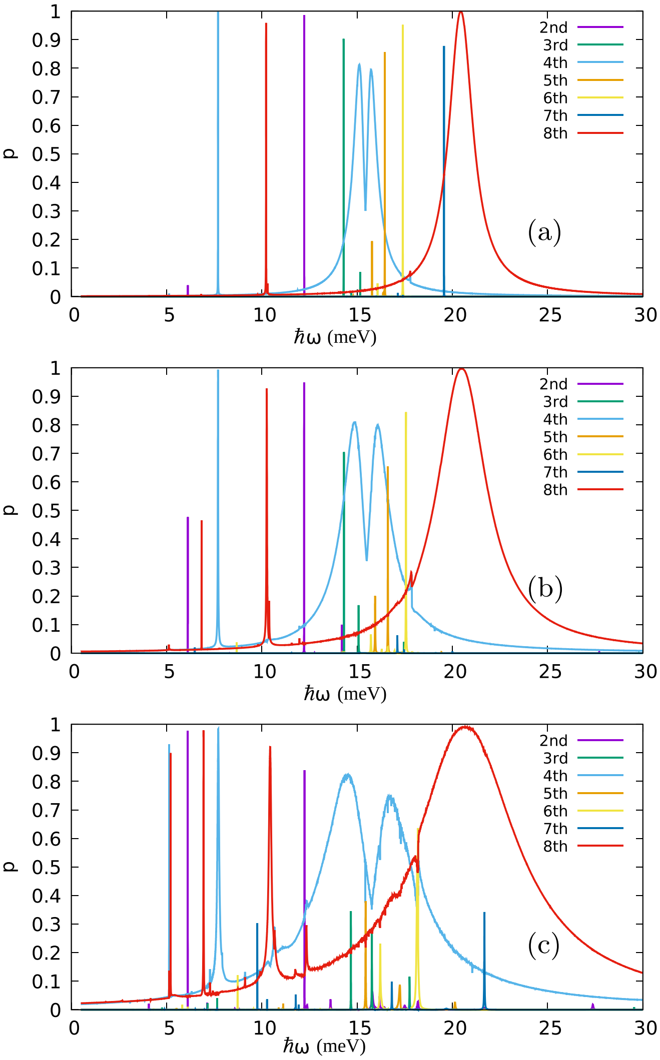

FIG. 9. The maximal occupation of the states for the simulation starting from the ground state and lasting 5 ns. Results for two electrons with Gaussian perturbation with $V_0 = 20$ meV and the AC field amplitude of 0.25 mV/nm (a), 0.5 mV/nm (b), and 1 mV/nm (c).

The first-order spin-flipping transitions can also be observed for an ideally parabolic confinement potential but with the in-plane magnetic field that lifts the Π symmetry. In Fig. 10(a), we plotted the two-electron spectrum as a function of the magnetic field oriented along the x axis with the structure of the lowest-energy excited state enlarged in Fig. 10(b). The value of the energies obtained at $B_x = 12$ T with the average spin x component and the transition matrix elements from the ground state are given in Table V. At $B_x = 12$ T, all the excited states considered in Table V are nearly twofold degenerate. The magnetic field–oriented in-plane does not produce the orbital effects present for the perpendicular magnetic field; hence, the splitting is primarily due to the SO interaction. The splitting of the excited energy levels is resolved in Fig. 10(b) with the exception of the two energy levels below −34.5 meV which, in the absence of the SO interaction, correspond to

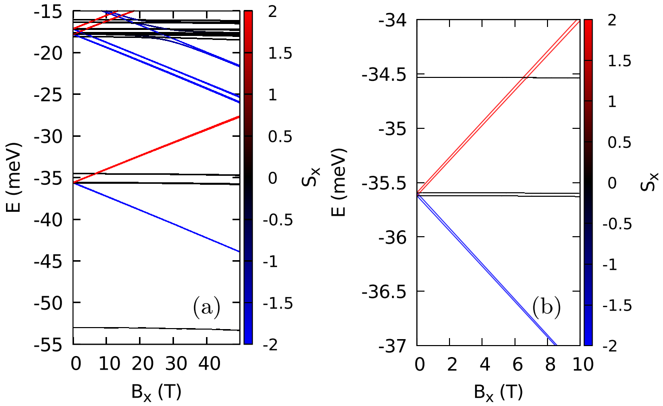

FIG. 10. The energy spectrum for two electrons with $\hbar\omega_0 = 18.688$ meV in the magnetic field oriented parallel to the x axis. (b) is a zoom of (a).

a spin singlet. All the other energy levels in Fig. 10(b) in the absence of SO coupling correspond to a spin triplet. For each couple of excited states, the transition matrix elements from the ground state are large for one of the states of the couple and much smaller for the other—see Table V. In the table, we see that the largest is the transition matrix element to an excited singlet state. The simulated spectra of excitations are plotted in Fig. 11 for the AC electric field oriented along the x axis with the amplitude (a) 0.25, (b) 0.5, and (c) 1 meV. The transition to the spin singlet—the seventh state—corresponds to the wide maximum, with the narrower peaks due to the third- and fifth-order processes (c) for the largest AC amplitude. We find that the spin-flip channels go through the first-order process for the second energy level and the second-order process for the third energy level. As the AC amplitude is increased, the peak corresponding to the second-order process increases, and the one due to the direct transition is reduced due to the strengthened presence of the seventh energy level in this excitation energy range. The spin-flip times for the AC amplitudes of 0.25, 0.5, and 1 mV/nm in the first-order transition to the second energy level are 2.4 ns, 1.1 ns, and 502 ps, with the fidelity of the transfer of 96.9, 89.3, and 75.6%, respectively. The corresponding numbers for the second-order transitions to the third state and the listed amplitudes are 11.67 ns, 3.03 ns, and 845 ps and 99.64, 99.54, and 98.48%, respectively.

TABLE V. The energy levels, the average value of S_x, and the transition matrix element for $B_x = 12$ T (see Fig. 10) with the AC field amplitude of 1 mV/nm.

n	$E + \Delta E$	$\langle S_x \rangle$	$\lvert eFx_{1n}\rvert$ (μeV)
1	−53.009	−0.001	0
2	−37.574	−1.993	3.42
3	−37.563	−1.990	0.021
4	−35.632	−0.000	0.049
5	−35.602	−0.001	12.228
6	−34.542	−0.000	4.630
7	−34.541	−0.001	3737.6
8	−33.686	1.992	9.046
9	−33.642	1.988	0.028

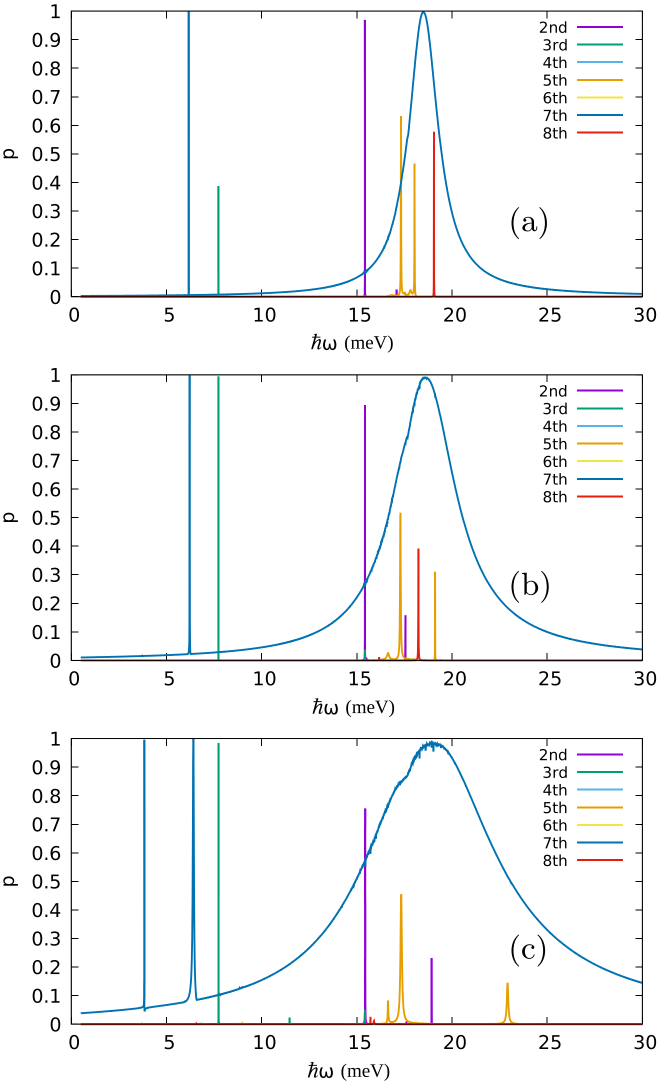

FIG. 11. The results for two electrons for confinement energy $\hbar\omega_0 = 18.688$ meV and the external magnetic oriented parallel to the x axis, $B_x = 12$ T. The maximal occupation of the states for the simulation starting from the ground state and lasting 5 ns is shown. The amplitude of the AC electric field oriented in the x direction is (a) 0.25, (b) 0.5, and (c) 1 mV/nm.

Like in the single-electron QD, now let us analyze what happens when $V_{\mathrm{AC}}(t)$ is set in the GHz regime. For a symmetric confinement potential and vertical magnetic field, the singlet-triplet first-order transition is forbidden by the parity selection rule. To set the spin-flip AC field frequency in the second-order process to ∼10 GHz, we need the singlet-triplet energy difference to be equal to $\sim 2 \times 0.0413$ meV. In the magnetic field range given in Fig. 6, this situation is observed only for the weakest confinement of $\hbar\omega_0 = 9.344$ meV, i.e., at $B_z = 25.4848$ T, just below the singlet-triplet crossing in Fig. 6(a). Figure 12(a) shows the maximal occupancy of the lowest-energy levels for the 5 ns time evolution in the AC field as a function of the driving frequency. The blueshift for this second-order process with the field amplitude is stronger than in the first-order process discussed above for the single electron. The fourth excited state (spin-singlet) participates

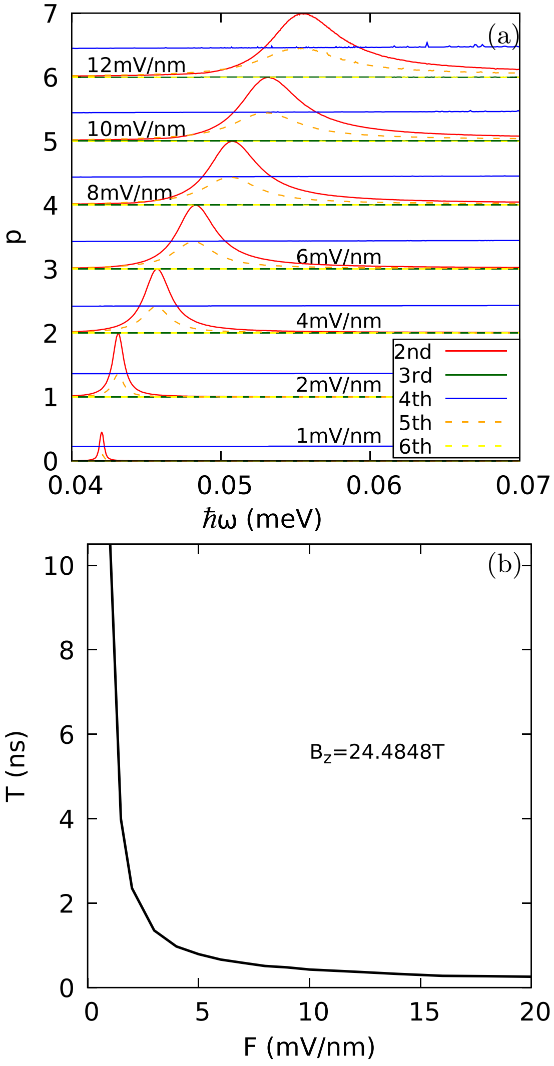

FIG. 12. The results for the two electrons and confinement energy $\hbar\omega_0 = 9.344$ meV at $B_z = 25.4848$ T. (a) The maximal occupancy of the lowest-energy levels for the time evolution lasting 5 ns starting from the spin-singlet ground state and AC field amplitude increasing from the bottom to the top. The subsequent plots for higher amplitudes are shifted by +1 each. (b) The singlet-triplet transition time as a function of the AC amplitude.

in the time evolution for all the considered amplitudes. The fifth excited state (spin-down polarized triplet) appears in the evolution near the resonance for the singlet-triplet transition. The spin-flip time can be taken from 10.6 ns (for $F = 1$ mV/nm) to 0.22 ns (for $F = 20$ mV/nm). The transitions are faster than in the single-electron case discussed above, but the magnetic field is two orders of magnitude larger.

Finally, as the considered QD is created electrostatically by the top and bottom gates, another issue which can be regarded is the possible application of the AC electric field perpendicular to the 2DEG using those gates. Although this specific scenario was not addressed in this paper, to delve into this situation further, three issues need to be raised:

(i) As stated in this paper, in the considered 2D model of a QD, the transition rate between the states with opposite spins depends on the relative orientation between the magnetic and electric fields—they need to be oriented in such a way that the effective SO magnetic field has a component perpendicular to the spin direction. For this reason, in our calculations, no transitions are observed when the magnetic field is directed along the y axis. In the case of the perpendicular electric field, the effective SO field is perpendicular to the spin orientation for the out-of-plane magnetic field. It means that the transitions between the spin states oriented in-plane should have a similar character as described in this paper.

(ii) The orbitals of d electrons are spatially oriented due to the vertical electric field. For this reason, we would expect that $d_{xz/yz}$ orbitals could play a more significant role for the perpendicular field orientation, leading to the increase of the transition elements between those orbitals.

(iii) The model considered in this paper is the projection of the real three-dimensional (3D) Hamiltonian into 2D x-y space, assuming that electrons occupy the ground state related to the confinement in the z direction. The transitions induced by a vertical AC field would involve excited states of the vertical quantization. Due to the nature of 2DEG, these excitations should require a large amount of energy. The description of these processes is, however, beyond the scope of this paper.

IV. SUMMARY AND CONCLUSIONS

We have studied single and two electrons confined in a lateral QD defined within the 2DEG on the (001)-oriented LAO/STO surface. For this purpose, we have developed a real-space tight-binding Hamiltonian spanned by 3D orbitals of Ti. The reduced Hamiltonian integrating the SO coupling effects due to the d_{xz} and d_{yz} orbitals into an effective in-plane d_{xy} band has also been derived and analyzed with respect to the full three-band model. We have analyzed the energy spectrum in a parabolic confinement and demonstrated that, for a weakly confined system, the low-energy eigenstates can be identified with the d_{xy} orbitals. In this case, the spectrum is close to the one of the harmonic oscillator with the electron effective mass of $m = 0.286m_0$. For stronger confinement, the states related to the orthogonal bands appear lower in the energy spectrum.

In this paper, we have discussed the manipulation of the confined spin by external AC voltages in the context of the EDSR and demonstrated that the spin flip in the ground state can be accomplished by a Rabi resonance with the transition time of the order of 0.5 ns for the amplitude of the AC field of the order of 1 mV/nm. For the electron pair in the harmonic oscillator potential and the perpendicular magnetic field, the singlet-triplet transition is forbidden by the parity symmetry. However, the spin flip can still be obtained via a second-order, two-photon process that has a two-state Rabi character for low AC field amplitude. The parity selection rule excluding the single-order transition can be lifted by a perturbation of the external potential or in-plane orientation of the external magnetic field. In this case, the first-order transition deviates from the Rabi oscillation due to the participation of higher-energy singlet states in the time evolution. We have also found that fidelity of the transfer increases when lowering the amplitude of the AC field and can reach ∼97% values. Our results can be verified in EDSR experiments on a LAO/STO QD [27]

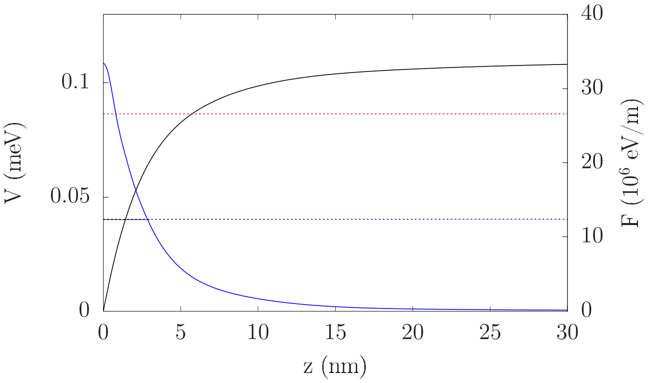

FIG. 13. Self-consistent potential profile at the LAO/STO interface (black line, left axis) together with the corresponding electric field (blue curve, right axis). Horizontal dashed lines mark the energy of the ground state for the d_{xy} (blue) and $d_{yz/xz}$ (red) orbitals.

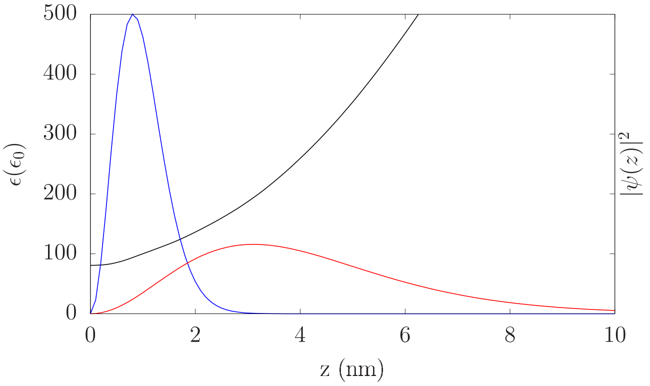

FIG. 14. The dielectric constant as a function of the position at the LAO/STO interface. The blue and red lines present a square of the wave function for the lowest-energy state of the vertical quantization for d_{xy} (blue) and $d_{xz/yz}$ (red) orbitals.

and demonstrate the possibility of quantum operation on oxide QDs with high fidelity and fast control.

ACKNOWLEDGMENTS

This paper was financed by the Horizon Europe EIC Pathfinder under "Spin-orbitronic quantum bits in reconfigurable 2D-oxides" (IQARO), Grant No. 101115190. Computing infrastructure PLGrid (HPC Center: ACK Cyfronet AGH) within computational Grant No. PLG/2023/016317 was used.

APPENDIX: DIELECTRIC CONSTANT AT THE LAO/STO INTERFACE

It is widely known that the dielectric constant of strontium titanate strongly depends on the temperature and electric field, reaching values as high as 10 000. However, it is important to note that the electric field near the interface where 2DEG is created is very strong, leading to a reduction in the dielectric constant [52]. To support our assumption regarding the relatively low value of ϵ at $\sim 100\epsilon_0$, we conducted additional calculations to determine the dielectric permittivity profile at the LAO/STO interface For this purpose, we employed the Schrödinger-Poisson approach, as detailed in Ref. [52], utilizing the spatially dependent $\epsilon(z)$ which varies according to the following formula, applicable for low temperatures:

$$\epsilon = \epsilon_0 + \frac{1}{A + B|F|}, \tag{A1}$$

where F is the electric filed, $A = 4.097 \times 10^{-5}$, $B = 4.907 \times 10^{-10}$ m/eV, and $\epsilon_0 = 70$. In the simulations, we took 2DEG electron density at the level 2×10^{13} cm^{-2}, while the trapped charge profile was assumed in such a way as to achieve an energy difference between the d_{xy} and $d_{xz/yz}$ ground states of $\sim$47 meV, as stated in this paper and experimentally measured [36].

In Fig. 13, we present the self-consistent potential profile showing that the electric field near the interface where 2DEG is embedded is significant. In this range of $\sim$10 nm, where wave functions of the ground state for the d_{xy} and $d_{xz/yz}$ orbitals are localized, the dielectric constant changes in the range $(80–200)\epsilon_0$ for the d_{xy} orbital and $(80–500)\epsilon_0$ for the $d_{xz/yz}$ orbital—see Fig. 14. As the main contribution to the electronic structure of a QD comes from the d_{xy} band, due to the shift of this band by 47 meV with respect to $d_{xz/yz}$, we assumed the dielectric constant equal to $100\epsilon_0$ as the average value of ϵ determined for this band. Furthermore, we confirmed that varying ϵ from $100\epsilon_0$ to $300\epsilon_0$ does not significantly affect our results.

[1] G. Burkard, T. D. Ladd, A. Pan, J. M. Nichol, and J. R. Petta, Rev. Mod. Phys. **95**, 025003 (2023).

[2] J. Medford, J. Beil, J. M. Taylor, E. I. Rashba, H. Lu, A. C. Gossard, and C. M. Marcus, Phys. Rev. Lett. **111**, 050501 (2013).

[3] F. H. L. Koppens, J. A. Folk, J. M. Elzerman, R. Hanson, L. H. W. van Beveren, I. T. Vink, H. P. Tranitz, W. Wegscheider, L. P. Kouwenhoven, and L. M. K. Vandersypen, Science **309**, 1346 (2005).

[4] F. H. L. Koppens, C. Buizert, K. J. Tielrooij, I. T. Vink, K. C. Nowack, T. Meunier, L. P. Kouwenhoven, and L. M. K. Vandersypen, Nature (London) **442**, 766 (2006).

[5] F. H. L. Koppens, K. C. Nowack, and L. M. K. Vandersypen, Phys. Rev. Lett. **100**, 236802 (2008).

[6] J. R. Petta, A. C. Johnson, J. M. Taylor, E. Laird, A. Yacoby, M. D. Lukin, C. M. Marcus, M. P. Hanson, and A. C. Gossard, Science **309**, 2180 (2005).

[7] S. Nadj-Perge, V. S. Pribiag, J. W. G. van den Berg, K. Zuo, S. R. Plissard, E. P. A. M. Bakkers, S. M. Frolov, and L. P. Kouwenhoven, Phys. Rev. Lett. **108**, 166801 (2012).

[8] M. D. Schroer, K. D. Petersson, M. Jung, and J. R. Petta, Phys. Rev. Lett. **107**, 176811 (2011).

[9] K. C. Nowack, F. H. L. Koppens, Y. V. Nazarov, and L. M. K. Vandersypen, Science **318**, 1430 (2007).

[10] S. Nadj-Perge, S. M. Frolov, E. P. A. M. Bakkers, and L. P. Kouwenhoven, Nature (London) **468**, 1084 (2010).

[11] Y. A. Bychkov and E. I. Rashba, J. Phys. C **17**, 6039 (1984).

[12] E. I. Rashba and A. L. Efros, Phys. Rev. Lett. **91**, 126405 (2003).
[13] V. N. Golovach, M. Borhani, and D. Loss, Phys. Rev. B **74**, 165319 (2006).
[14] M. P. Nowak, B. Szafran, and F. M. Peeters, Phys. Rev. B **86**, 125428 (2012).
[15] D. V. Khomitsky, E. A. Lavrukhina, and E. Y. Sherman, Phys. Rev. B **99**, 014308 (2019).
[16] D. V. Khomitsky, E. A. Lavrukhina, and E. Y. Sherman, Phys. Rev. Appl. **14**, 014090 (2020).
[17] C. Cen, S. Thiel, J. Manhart, and J. Levy, Science **323**, 1026 (2009).
[18] A. Ohtomo and H. Y. Hwang, Nature (London) **427**, 423 (2004).
[19] A. D. Caviglia, M. Gabay, S. Gariglio, N. Reyren, C. Cancellieri, and J.-M. Triscone, Phys. Rev. Lett. **104**, 126803 (2010).
[20] C. Yin, P. Seiler, L. M. K. Tang, I. Leermakers, N. Lebedev, U. Zeitler, and J. Aarts, Phys. Rev. B **101**, 245114 (2020).
[21] E. Maniv, M. Ben Shalom, M. Mograbi, A. Pavelski, M. Goldstein, and Y. Dagan, Nat. Commun. **6**, 8239 (2015).
[22] A. M. R. V. L. Monteiro, M. Vivek, D. J. Groenendijk, P. Bruneel, I. Leermakers, U. Zeitler, M. Gabay, and A. D. Caviglia, Phys. Rev. B **99**, 201102(R) (2019).
[23] A. Joshua, S. Pecker, J. Ruhman, E. Altman, and S. Ilani, Nat. Commun. **3**, 1129 (2012).
[24] J. Biscaras, N. Bergeal, S. Hurand, C. Grossetête, A. Rastogi, R. C. Budhani, D. LeBoeuf, C. Proust, and J. Lesueur, Phys. Rev. Lett. **108**, 247004 (2012).
[25] N. Pavlenko, T. Kopp, E. Y. Tsymbal, G. A. Sawatzky, and J. Mannhart, Phys. Rev. B **85**, 020407(R) (2012).
[26] P. Noël, F. Trier, L. M. Vicente Arche, J. Bréhin, D. C. Vaz, V. Garcia, S. Fusil, A. Bathélémy, L. Vila, M. Bibes *et al.*, Nature (London) **580**, 483 (2020).
[27] A. V. Bjørlig, D. J. Carrad, G. E. D. K. Prawiroatmodjo, M. von Soosten, Y. Gan, Y. Chen, N. Pryds, J. Paaske, and T. S. Jespersen, Phys. Rev. Mater. **4**, 122001(R) (2020).
[28] H. Thierschmann, E. Mulazimoglu, N. Manca, S. Goswami, T. M. Klapwijk, and A. D. Caviglia, Nat. Commun. **9**, 2276 (2018).
[29] E. Guenevere, M. Leijnse, F. Trier, Y. Chen, D. V. Christensen, M. von Soosten, N. Pryds, and T. S. Jespersen, Nat. Commun. **8**, 395 (2017).
[30] A. Jouan, G. Singh, E. Lesne, D. C. Vaz, M. Bibes, A. Barthélémy, C. Ulysse, D. Stornaiuolo, M. Salluzzo, S. Hurand *et al.*, Nat. Electron. **3**, 201 (2020).
[31] A. V. Khaetskii, D. Loss, and L. Glazman, Phys. Rev. Lett. **88**, 186802 (2002).
[32] E. Lesne, Y. Fu, S. Oyarzun, J. C. Rojas-Sánchez, D. C. Vaz, H. Naganuma, G. Sicoli, J.-P. Attané, M. Jamet, E. Jacquet *et al.*, Nat. Mater. **15**, 1261 (2016).
[33] D. C. Vaz, P. Noël, A. Johansson, B. Göbel, F. Y. Bruno, G. Singh, S. McKeown-Walker, F. Trier, L. M. Vicente-Arche, A. Sander *et al.*, Nat. Mater. **18**, 1187 (2019).
[34] M. Trama, V. Cataudella, C. A. Perroni, F. Romeo, and R. Citro, Phys. Rev. B **106**, 075430 (2022).
[35] M. Trama, C. A. Cataudella, V. Perroni, F. Romeo, and R. Citro, Nanomaterials **12**, 2494 (2022).
[36] E. Maniv, A. Ron, M. Goldstein, A. Palevski, and Y. Dagan, Phys. Rev. B **94**, 045120 (2016).
[37] Z. S. Popović, S. Satpathy, and R. M. Martin, Phys. Rev. Lett. **101**, 256801 (2008).
[38] R. Pentcheva and W. E. Pickett, Phys. Rev. B **74**, 035112 (2006).
[39] M. Diez, A. M. R. V. L. Monteiro, G. Mattoni, E. Cobanera, T. Hyart, E. Mulazimoglu, N. Bovenzi, C. W. J. Beenakker, and A. D. Caviglia, Phys. Rev. Lett. **115**, 016803 (2015).
[40] G. Khalsa, B. Lee, and A. H. MacDonald, Phys. Rev. B **88**, 041302(R) (2013).
[41] J. Ruhman, A. Joshua, S. Ilani, and E. Altman, Phys. Rev. B **90**, 125123 (2014).
[42] S. Giglberger, L. E. Golub, V. V. Bel'kov, S. N. Danilov, D. Schuh, C. Gerl, F. Rohlfing, J. Stahl, W. Wegscheider, D. Weiss *et al.*, Phys. Rev. B **75**, 035327 (2007).
[43] S. Gariglio, A. Féte, and J.-M. Triscone, J. Phys.: Condens. Matter **27**, 283201 (2015).
[44] K. A. Guerrero-Becerra and M. Rontani, Phys. Rev. B **90**, 125446 (2014).
[45] M. P. Nowak and B. Szafran, Phys. Rev. B **89**, 205412 (2014).
[46] A. Noiri, K. Takeda, T. Nakajima, T. Kobayashi, A. Sammak, G. Scappucci, and S. Tarucha, Nature (London) **601**, 338 (2022).
[47] A. M. Ferrenti, N. P. de Leon, J. D. Thompson, and R. J. Cava, npj Comput Mater **6**, 126 (2020).
[48] E. N. Osika, A. Mreńca, and B. Szafran, Phys. Rev. B **90**, 125302 (2014).
[49] S. Bednarek and B. Szafran, Phys. Rev. Lett. **101**, 216805 (2008).
[50] D. V. Khomitsky, L. V. Gulyaev, and E. Y. Sherman, Phys. Rev. B **85**, 125312 (2012).
[51] J. H. Shirley, Phys. Rev. **138**, B979 (1965).
[52] N. Scopigno, D. Bucheli, S. Caprara, J. Biscaras, N. Bergeal, J. Lesueur, and M. Grilli, Phys. Rev. Lett. **116**, 026804 (2016).